Thermal and magnetic properties of integrable spin-1 and spin-$\frac{3}{2}$ chains with applications to real compounds

M. T. Batchelor[†], **X.-W. Guan**[†], **N. Oelkers**[†] **and A. Foerster**[‡]

[†] Department of Theoretical Physics, Research School of Physical Sciences & Engineering, and Mathematical Sciences Institute,
Australian National University, Canberra ACT 0200, Australia
[‡] Instituto de Fisica da UFRGS, Av. Bento Goncalves, 9500,
Porto Alegre, 91501-970, Brazil

Abstract. The ground state and thermodynamic properties of spin-1 and spin-$\frac{3}{2}$ chains are investigated via exactly solved $su(3)$ and $su(4)$ models with physically motivated chemical potential terms. The analysis involves the Thermodynamic Bethe Ansatz and the High Temperature Expansion (HTE) methods. For the spin-1 chain with large single-ion anisotropy, a gapped phase occurs which is significantly different from the valence-bond-solid Haldane phase. The theoretical curves for the magnetization, susceptibility and specific heat are favourably compared with experimental data for a number of spin-1 chain compounds. For the spin-$\frac{3}{2}$ chain a degenerate gapped phase exists starting at zero external magnetic field. A middle magnetization plateau can be triggered by the single-ion anisotropy term. Overall, our results lend further weight to the applicability of integrable models to the physics of low-dimensional quantum spin systems. They also highlight the utility of the exact HTE method.

PACS numbers: 75.10.Pq, 75.10.Jm, 64.60.Cn

Contents

1. Introduction

This paper is concerned with the study of two integrable quantum spin chains. By integrable we mean that the chains are exactly solvable in the non-diffractive [1] Yang-Baxter sense [2, 3], with infinitely many conserved quantities and an underlying Bethe Ansatz solution. The two particular models are variants of the spin-1 and spin-$\frac{3}{2}$ chains based on the family of integrable su(n) permutator models [4, 5]. The two-dimensional classical lattice model counterparts are the A_{n-1} models [6, 7], aka the Perk-Schultz model [8] in a special case.

Over the past few decades considerable effort has been invested in the analysis of exactly solved models in statistical mechanics [9, 10]. Of particular relevance here is the calculation of the temperature-dependent properties [11]. This began with the Thermodynamic Bethe Ansatz (TBA) approach [12, 13] and has most recently evolved into the exact High Temperature Expansion (HTE) method [14, 15]. The key ingredients of the HTE method are the Quantum Transfer Matrix (QTM) [16, 17] and the T-system [18], from which one derives nonlinear integral equations which can be solved in an exact perturbative fashion. To date this approach has been applied to the Heisenberg model [14], the *su(n)* models [15], the higher spin Heisenberg model [19] and to integrable quantum spin ladders [20, 21]. In particular, it has been demonstrated that integrable models can be used to study real ladder compounds [20]. On the one hand, the TBA method was seen to be most convenient for predicting critical fields [22, 23, 24] of relevance to the quantum phase transitions in ladder compounds. On the other hand, the HTE method gave the temperature-dependent free energy, from which physical properties such as the magnetic susceptibility and the specific heat were derived. Excellent agreement between the theoretical and experimental results for the strong coupling ladder compounds has been found [20].

Here we apply the TBA and HTE methods to calculate the thermal and magnetic properties of spin-1 and spin-$\frac{3}{2}$ chains.‡

1.1. Physical motivation

Low-dimensional spin systems continue to reveal rich and novel quantum magnetic effects, such as fractional magnetization plateaux [26, 27] and spin-Peierls transitions [28]. The effects of inter- and intra-chain interactions, single-ion anisotropy, biquadratic exchange interactions and the magnetic field all provide competing contributions in the low-temperature physics. As an example consider the spin-S Heisenberg chain [29]: if $2S$ is odd, the next-nearest-neighbour exchange interaction and anisotropy may drive the chain into either a non-magnetic singlet ground state (spin-Peierls transition) [28] or a magnetic gapped ground state [30]. Conversely, if $2S$ is even the Haldane gap may be closed in the presence of additional biquadratic terms or in-plane anisotropy. In general, the Haldane phase exists only in $2S$ even Heisenberg chains with antiferromagnetic

‡ A brief account of our results can be found in Ref. [25].

coupling, no gap appears in ferromagnetic Heisenberg chains. Accordingly one expects a rich quantum phase diagram to emerge for low-dimensional spin chains. More specifically, the intra- and inter-chain exchange interactions may result in either a valence-bond-solid Haldane phase or a dimerized phase [31], whereas large single-ion anisotropy may trigger a field-induced gapped phase [30, 32] significantly different from the standard Haldane phase.

The spin-1 Heisenberg chain has been extensively studied in the context of Haldane gapped materials [33, 34, 35, 36, 37]. Recently an anomaly in the susceptibility has been observed in the spin-1 compounds $LiVGe_2O_6$ [38]. Such new materials have drawn attention from both theorists and experimentalists [39, 40, 41]. The Heisenberg spin-1 chain with additional biquadratic interaction has also been studied with regard to the Haldane phase [41, 42]. In particular, the susceptibility of $LiVGe_2O_6$ can be quantitatively explained with the spin-1 bilinear-biquadratic chain [38, 41]. On the other hand, a field-theoretic approach to the Heisenberg spin-1 chain with single-ion anisotropy was suggested by Tsvelik [32]. His theoretical predictions are in good agreement with experimental results for the compound $Ni(C_2H_8N_2)NO_2ClO_4$.

1.2. Application to real compounds

The Haldane gapped phase is observed in some one-dimensional materials exhibiting a weak single-ion anisotropy D, such that $D \leq J$, where J is the nearest-neighbour exchange interaction. However, a large anisotropy ($D > J$) can also produce a gapped phase [30], which is significantly different from the Haldane phase found in weakly anisotropic compounds. In this latter case, the Haldane nondegenerate ground state is a valence-bond solid state [31] in which a single valence bond connects each neighbouring pair to form a singlet. An expected excitation from the valence-bond solid state arises from a configuration in which a nonmagnetic state $S_i = 0$ at site i is substituted for a state with $S_i = 1$. In this way a total spin-1 excitation creates an energy referred to as the energy gap. However, bond alternation may lead to a dimerized ground state in which double valence bonds form two singlets between pairs of neighboring spins. By breaking one dimer with a nonmagnetic state at site i, a total spin-1 excitation is also separated.

On the other hand, the field-induced gapped phase in the spin-1 chain is caused by trivalent orbital splitting, i.e., the singlet and doublet orbitals are separated by a crystal-field splitting. The singlet can occupy all states such that the ground state lies in the nondegenerate gapped phase. The lowest excitation arises as the doublet becomes involved in the ground state. This gapped phase is observed in some Nickel salts with large zero-field splitting, such as $NiSnCl_6 \cdot 6H_2O$ [43], $[Ni(C_5H_5NO)_6](ClO_4)_2$ [44] and $Ni(NO_3)_2 \cdot 6H_2O$ [45]. Recently, other spin-1 magnetic compounds:

 (i) $Ni(C_2H_8N_2)_2Ni(CN)_4$ (abbreviated NENC)[46, 47, 48],

 (ii) $Ni(C_{11}H_{10}N_2O)_2Ni(CN)_4$ (abbreviated as NDPK) [46], and

(iii) $Ni(C_{10}H_8N_2)_2Ni(CN)_4 \cdot H_2O$ (abbreviated NBYC) [46, 49],

have also been identified as effective Heisenberg magnetic chains. This class of compounds exhibits a nondegenerate ground state which can be separated from the lowest excitation. Theoretical studies of these compounds have relied on a molecular field approximation via the Van Vleck equation [50]. To first order Van Vleck approximation the exchange interaction is neglected and an effective crystalline field is incorporated to fit the experimental data. Not surprisingly these approximations cause some discrepancies in fitting the data. Although there has been some theoretical interpretation, the nature of the quantum phase transitions as well as the general microscopic Hamiltonian remains to be fully clarified for these compounds.

1.3. Results and outline of this paper

In this paper we consider integrable one-dimensional spin-1 and spin-$\frac{3}{2}$ models with large planar single-ion anisotropy. We find that for the integrable spin-1 chain the non-magnetic singlet and the magnetic doublet states can be separated from the lowest magnon excitation by an energy gap. A large single-ion anisotropy together with in-plane anisotropy may trigger a non-magnetic mid-plateau, leading to a "ferrimagnetic-antiferromagnetic" phase transition. Significantly, a different type of gapped phase compared to the standard Haldane phase is found. We examine some real spin-1 compounds via TBA and HTE. Excellent agreement between our theoretical predictions and the experimental results for spin-1 compounds such as Nickel salts and magnetic chains (NENC, NBYC and NDPK) is found. Our results show that the strong single-ion anisotropy, which is induced by an orbital splitting, can dominate the behaviour of these compounds.

For the integrable spin-$\frac{3}{2}$ chain the magnetic gapped ground state can be separated from the lowest magnon excitation, in contrast to the non-magnetic Haldane gapped phase in the spin-1 chain. A magnetization plateau at $M = \frac{1}{2}$ originates at zero magnetic field. Moreover, an appropriately chosen value of the anisotropy can open a one third magnetization plateau reminiscent of the mixed spin-$(1, \frac{1}{2})$ ladder model [23].

The paper is organized as follows. In section 2 we introduce the integrable su(3) spin-1 chain and briefly review its exact solution. Then in section 2.3 we discuss the ground state properties via the TBA. In section 2.4 we derive the high temperature magnetic properties via the HTE method. We then discuss the application of the TBA and the HTE methods to real spin-1 materials with single-ion and in-plane anisotropies in section 3. In particular, we examine the thermal and magnetic properties of the Nickel salt $NiSnCl_6 \cdot 6H_2O$ (section 3.1) and the magnetic chains NENC (section 3.2), NBYC (section 3.3) and NDPK (section 3.4) by comparing our TBA and HTE results with the experimental data for the specific heat, magnetic susceptibiliy and magnetization, where available. In section 4 we apply the same approach to the su(4) case in the context of the integrable spin-$\frac{3}{2}$ chain. Concluding remarks are given in section 5.

2. The integrable spin-1 chain

2.1. The Heisenberg spin-1 chain

Initially, the Haldane gap was identified in some quasi one-dimensional spin-1 materials [34, 35, 36] described by the Heisenberg Hamiltonian

$$\mathcal{H} = J \sum_{j=1}^{L} \vec{S}_j \cdot \vec{S}_{j+1} + D \sum_{j=1}^{L} (S_j^z)^2 - \mu_B g H \sum_{j=1}^{L} S_j^z \tag{1}$$

in a parallel external magnetic field H. Here $\vec{S}_i$ denotes the spin-1 operator at site i and L is the number of sites. The constants J and D denote the exchange spin-spin coupling strength and single-ion anisotropy, respectively. The Bohr magneton is denoted by μ_B and g is the Lande factor. For the compound NENP [36] the energy gap Δ between the ground state and the first excited state is of magnitude $\Delta \approx 12$ K with the coupling constants $J = 48$ K and $D = 0.2J$. While for the compound NINO [34], $\Delta \approx 10 - 15$ K with $J = 52$ K and $D = 0.3J$. The above Hamiltonian has been recognized as a good model for Haldane-like compounds and has thus found widespread interest in the theoretical community [26, 51, 52]. Unfortunately it does not appear to be integrable. However, if the spin-spin interaction term is changed, the model is integrable, and thus amenable to exact calculations using the sophisticated and well developed machinery of integrable models. We shall see below that under favourable conditions the modified Hamiltonian exhibits similar physical behaviour.

2.2. The integrable su(3) spin-1 chain

We consider the Hamiltonian

$$\mathcal{H} = J \sum_{j=1}^{L} \left(\vec{S}_j \cdot \vec{S}_{j+1} + \left(\vec{S}_j \cdot \vec{S}_{j+1} \right)^2 \right) + \mathcal{H}_{\text{chem.pot}} \tag{2}$$

which only differs from the Heisenberg Hamiltonian (1) in the additional biquadratic interaction term.§ We discuss the on-site chemical potential terms $\mathcal{H}_{\text{chem.pot}}$ in detail further below. Leaving aside $\mathcal{H}_{\text{chem.pot}}$, the model (2) is the integrable $su(3)$ spin-1 chain, which is well understood [53, 54]. It belongs to a family of solvable models with Lie algebra $su(n)$ symmetry, which are generalized multi-state vertex models [7, 55]. The spin-1 chain was originally considered by Uimin [4] in 1970 and later in the context of multi-state permutation operators by Sutherland [5]. A key ingredient is the identity [4]

$$P_{i,j} = \vec{S}_i \cdot \vec{S}_j + \left(\vec{S}_i \cdot \vec{S}_j \right)^2 - \mathbf{I}_i \otimes \mathbf{I}_j, \tag{3}$$

§ There are in fact three integrable $su(2)$-invariant spin-1 Hamiltonians, each involving biquadratic interactions [53]. Only the model considered here, with two-body interactions based on the permutation operator, appears to allow the desired chemical potential terms.

where $\mathbf{I}$ is the identity operator. We are thus considering the model

$$\mathcal{H} = J \sum_{i=1}^{L} P_{i,i+1} + \mathcal{H}_{\text{chem.pot}} \tag{4}$$

acting on $V^{\otimes L}$ where V is a three-dimensional vector space and $P_{i,i+1}$ is the permutation operator, acting trivially on all sites, except sites i and $i+1$, where

$$P_{i,i+1}|j_1, j_2, \ldots, \underbrace{j_i, j_{i+1}}, \ldots, j_L\rangle = |j_1, j_2, \ldots, \underbrace{j_{i+1}, j_i}, \ldots, j_L\rangle. \tag{5}$$

We take the spin-spin exchange interaction J to be antiferromagnetic $(J > 0)$.

A crucial point in the following TBA and HTE analysis is the observation that the form of the permutation operator is not dependent on which basis spans V. Accordingly we always choose a local basis which diagonalizes the chemical potential terms. The chemical potentials characterize physical on-site interaction terms in the model Hamiltonian. Fortunately there is freedom to adjust them without losing integrability.

To simplify the Bethe Ansatz, we apply periodic boundary conditions, i.e., we identify $P_{L,L+1} = P_{L,1}$ and $V_{L+1} = V_1$. Following the standard approach this model can be solved by the nested Bethe Ansatz [4, 5], which gives the energy eigenvalues

$$\mathcal{E} = -J \sum_{j=1}^{M_1} \frac{1}{(v_j^{(1)})^2 + \frac{1}{4}} + N_1 \mu_1 + N_2 \mu_2 + N_3 \mu_3 \tag{6}$$

in terms of Bethe roots of flavour/colour $v_j^{(i)}$. Only the Bethe roots of first flavour $v_j^{(1)}$ appear in the energy expression. The roots are determined by solutions to the Bethe equations

$$\left(\frac{v_j^{(1)} + \frac{1}{2}\mathrm{i}}{v_j^{(1)} - \frac{1}{2}\mathrm{i}} \right)^L = \prod_{\substack{l=1 \\ l \neq j}}^{M_1} \frac{v_j^{(1)} - v_l^{(1)} + \mathrm{i}}{v_j^{(1)} - v_l^{(1)} - \mathrm{i}} \prod_{l=1}^{M_2} \frac{v_j^{(1)} - v_l^{(2)} - \frac{1}{2}\mathrm{i}}{v_j^{(1)} - v_l^{(2)} + \frac{1}{2}\mathrm{i}},$$

$$\prod_{i=1}^{M_1} \frac{v_k^{(2)} - v_i^{(1)} + \frac{1}{2}\mathrm{i}}{v_k^{(2)} - v_i^{(1)} - \frac{1}{2}\mathrm{i}} = \prod_{\substack{l=1 \\ l \neq k}}^{M_2} \frac{v_k^{(2)} - v_l^{(2)} + \mathrm{i}}{v_k^{(2)} - v_l^{(2)} - \mathrm{i}}, \tag{7}$$

where $j = 1, 2, \ldots, M_1$ and $k = 1, 2, \ldots, M_2$.

In eq. (6) N_i denotes the occupation number of sites in state $|i\rangle$ for $i = 1, 2, 3$, where the basis $|1\rangle, |2\rangle, |3\rangle$ diagonalizes the chemical potential term under consideration with eigenvalues μ_1, μ_2, μ_3. The Bethe quantum numbers M_1 and M_2, satisfying $0 \leq M_2 \leq M_1 \leq L$, are related to the number of sites in state $|i\rangle$ by

$$
\begin{aligned}
N_1 &= L - M_1, \\
N_2 &= M_1 - M_2, \\
N_3 &= M_2.
\end{aligned} \tag{8}
$$

The solution (6) in terms of the Bethe equations (7) is valid for any permutation of the basis order. We do not specify the basis here, rather we are free to choose the *order* of

the basis and we will exploit this in the TBA analysis of the ground state, as done in the TBA analysis of the integrable ladder models [22, 23, 24, 56].

2.2.1. Chemical potential terms We choose the chemical potential terms which most closely model the physics of the compounds as used in the literature. The most general chemical potential terms exhibited in the real compounds are of the form

$$\mathcal{H}_{\text{chem.pot}} = -\mu_B g H_z \sum_{j=1}^{L} S_j^z + D \sum_{j=1}^{L} (S_j^z)^2 + E \sum_{j=1}^{L} \left((S_j^x)^2 - (S_j^y)^2 \right), \qquad (9)$$

$$\mathcal{H}_{\text{chem.pot}} = -\mu_B g H_x \sum_{j=1}^{L} S_j^x + D \sum_{j=1}^{L} (S_j^z)^2 + E \sum_{j=1}^{L} \left((S_j^x)^2 - (S_j^y)^2 \right). \qquad (10)$$

The first term in each equation describes the effect of an external magnetic field H, which can be applied either parallel or perpendicular to the quantization axis given by the sample geometry. The in-plane anisotropy and planar anisotropy effects may be detected in magnetic properties of a single crystal. Actually, we can transform the transverse external magnetic field H_x in (10) to the z direction via the following equivalent chemical potentials

$$\mathcal{H}_{\text{chem.pot}} = -\mu_B g H_z \sum_{j=1}^{L} S_j^z + D \sum_{j=1}^{L} (S_j^x)^2 + E \sum_{j=1}^{L} \left((S_j^z)^2 - (S_j^y)^2 \right). \qquad (11)$$

Therefore, the magnetic field perpendicular to the quantized axis provides a way to examine thermodynamic properties for the powdered samples via the chemical potentials (11). We will assume that $D > 0$ and interpret it as a planar/single-ion anisotropy modelling the effect of crystal-field splitting. The third contribution describes an in-plane anisotropy effect which breaks the z^2 symmetry. We consider only the case $E \geq 0$.

Although we do not need to consider the (complicated) eigenbasis of the chemical potential terms (9) or (10) in performing the algebraic Bethe ansatz and applying the HTE method, the eigenbasis for different chemical potentials is helpful in analyzing the ground state properties of the Hamiltonian (2). The eigenbasis could for instance be presented as linear combinations of the spin projection onto the z-axis eigenstates $|S^z = \pm 1, 0\rangle$ where the coefficients are dependent on H, D and E. The eigenbasis for the Hamiltonian (2) with different chemical potentials will be given in the following TBA analysis. The eigenvalues of the chemical potentials are given by

$$\mu_1 = -\sqrt{E^2 + (\mu_B g H)^2}, \qquad (12a)$$

$$\mu_2 = -D, \qquad (12b)$$

$$\mu_3 = \sqrt{E^2 + (\mu_B g H)^2}, \qquad (12c)$$

$$\mu_1 = -\frac{1}{2}\left(D - E + \sqrt{(D+E)^2 + (2\mu_B g H)^2} \right), \qquad (12d)$$

$$\mu_2 = -E, \qquad (12e)$$

$$\mu_3 = -\frac{1}{2}\left(D - E - \sqrt{(D+E)^2 + (2\mu_B g H)^2} \right) \qquad (12f)$$

for (9) and (10), respectively.

Note that we can adjust the chemical potential terms to model the physics of a specific compound without losing integrability, but we have no freedom in changing the spin-spin exchange interaction fixed by the permutation identity (3). In this way, the integrable $su(3)$ chain (2) may describe some real compounds having either a spin-spin interaction close to the permutation interaction or exhibiting a strong single-ion anisotropy which effectively dominates the intrachain exchange interaction in the ground state. Fortunately, compounds are known where the relative strength J/D or J/E are very small. Thus the planar and in-plane anisotropies tend to dominate the physics.

A large D anisotropy may trigger a gapped phase where the singlet occupies the whole ground state. In such a phase, the Bethe reference state becomes the true physical ground state, with Bethe numbers M_1 and M_2 in the Bethe equations (7) equal to zero. The lowest excitation arises from a configuration in which the doublet is involved in the ground state. This excitation gives the energy gap, which can be caculated either from the energy (6) in terms of the Bethe equations (7) or from the TBA equations. We shall see that both the magnetic field and the in-plane anisotropy decrease the energy gap.

2.3. TBA analysis: Ground state properties

We consider the thermodynamic limit in which the Bethe equations (7) have different types of solutions. The real roots, called magnons, form the ground state. Pairs of complex conjugated roots form bound states of two magnons. There are many kinds of bound states. The so-called string hypothesis was developed to classify such excitations, for example, for the one-dimensional boson gas with delta interaction [12], the Heisenberg chain [13], the Hubbard model [57], the supersymmetric $t - J$ model [58] and the Kondo model [59]. Applying the string hypothesis it is quite standard to derive the TBA equations

$$\ln(1 + \eta_n^{(1)}) = \frac{1}{T}g_n^{(1)} + \sum_{m=1}^{\infty} A_{nm} * \ln(1 + \eta_m^{(1)-1}) - \sum_{m=1}^{\infty} a_{nm} * \ln(1 + \eta_m^{(2)-1}),$$

$$\ln(1 + \eta_n^{(2)}) = \frac{1}{T}g_n^{(2)} + \sum_{m=1}^{\infty} A_{nm} * \ln(1 + \eta_m^{(2)-1}) - \sum_{m=1}^{\infty} a_{nm} * \ln(1 + \eta_m^{(1)-1}), \quad (13)$$

from (7) in a lengthy procedure [13, 12, 58, 22, 23, 24]. We use the conventional notation, with

$$a_n(v) = \frac{1}{2\pi} \frac{n}{n^2/4 + v^2} \quad (14)$$

and the convolution denoted by $*$. The densities of roots and holes are $\rho_n^{(k)}(v)$ and $\rho_n^{(k)h}(v)$, for $k = 1, 2$ with $\eta_n^{(k)} = \rho_n^{(k)h}(\lambda)/\rho_n^{(k)}(\lambda)$ for $n = 1, 2, 3, \ldots$. The driving terms $g_n^{(k)}$ depend on the choice of eigenbasis. We give them below for different configurations, i.e., we will permute the basis order to enable the simplest analysis of different regions in the parameter space (H, D, E).
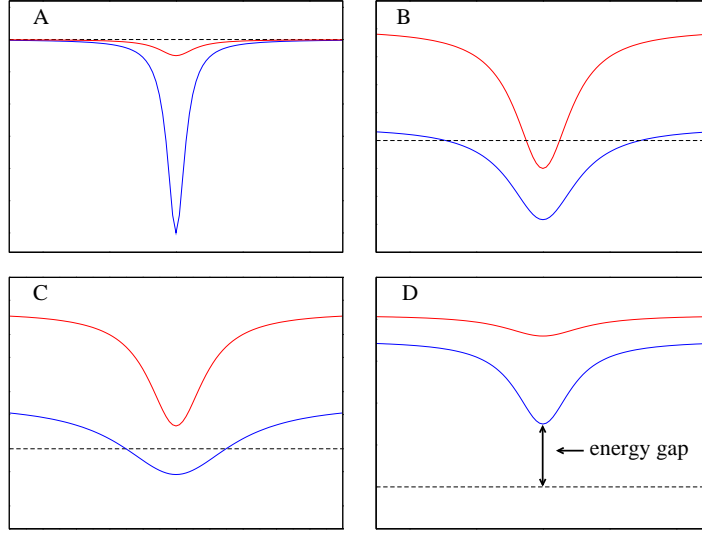
Figure 1. Dressed energies for the su(3)-based TBA equations (15). In each case the horizontal axis is the spectral parameter v with the origin ($v = 0$) at the minima. The vertical axis carries the dressed energies. Due to our basis reordering the upper graph (red) is always the current second excitation $\epsilon^{(2)}$ while the lower graph is the first excitation $\epsilon^{(1)}$. The Fermi energy for both flavours is always $\epsilon_F = 0$, denoted by the dotted line. Shown are the four typical cases of solutions to (15): (A) no chemical potentials, (B) mixed state involving all three basis states, (C) gap in $\epsilon^{(2)}$ and (D) gapped ground state with energy gap Δ (see text in section 2.3).

We define the so-called *dressed energies* $\epsilon_n^{(k)}$ via $\eta_n^{(k)} := \exp(\epsilon_n^{(k)}(\lambda)/T)$ with $k = 1, 2$. They play the role of excitation energies, measured from the Fermi energy level for each flavour and satisfy Fermi statistics. In the limit $T \to 0$, only the negative part of the dressed energies, $\epsilon^{(l)-} := \min(\epsilon^{(l)}, 0)$, contributes to the ground state energy. Thus the TBA equations (13) reduce to two coupled nonlinear integral equations

$$\epsilon^{(1)} = g_1 + a_1 * \epsilon^{(2)-} - a_2 * \epsilon^{(1)-},$$
$$\epsilon^{(2)} = g_2 + a_1 * \epsilon^{(1)-} - a_2 * \epsilon^{(2)-}. \tag{15}$$

The solution of these equations provides a clear physical picture of the ground state properties.

For typical solutions to (15) see Figure 1. To simplify the analysis of (15) we separate the calculations for regions in parameter space where the basis order changes in accordance with the energy levels of the chemical potentials. The assignment $|a\rangle$ with $a = 1, 2, 3$ naturally depends on the parameters H, D and E, which change the energy level of the chemical potentials (as, e.g., in Figure 4). The driving terms g_i are then positive or negative in defined regions [22, 23, 24] allowing for a simple determination of critical fields and gaps. The band fillings are controlled by these driving terms. In the absence of symmetry-breaking potentials all bands are completely filled, i.e., their Fermi bundaries are their value at infinity, with $\epsilon(\infty) = \epsilon_F$.

2.3.1. $D > 0$, $E > 0$ In this part of the TBA analysis we discuss the most general Hamiltonian with both anisotropies, $D > 0$ and $E > 0$, with an external parallel magnetic field H. In later sections we specialize to cases without in-plane anisotropy to model certain physical compounds. The perpendicular magnetic field term (10) with eigenvalues (12d)-(12f) can be treated in the same manner. But the in-plane and planar anisotropies play different roles under perpendicular and parallel magnetic fields.

Starting with Hamiltonian (2) without chemical potentials, i.e. with $\mu = 0$, where the model has $su(3)$ symmetry with the fundamental basis $|1\rangle = |+1\rangle$, $|2\rangle = |0\rangle$ and $|3\rangle = |-1\rangle$. The energy eigenvalue is threefold degenerate. The single-ion anisotropy term $D(S_j^z)^2$ breaks this symmetry into a doublet and a singlet $(su(2) \oplus u(1))$. The fundamental basis is still an eigenbasis as the z direction is the axis of quantization. Turning on the external magnetic field, this symmetry is further broken into $u(1) \oplus u(1) \oplus u(1)$. However, the in-plane anisotropy E breaks the z^2 symmetry even for $H = 0$. The energies split into three levels with respect to the anisotropy and magnetic field. The new basis, $|1\rangle = a_-|-1\rangle + |+1\rangle$, $|2\rangle = |0\rangle$ and $|3\rangle = a_+|-1\rangle + |+1\rangle$, with $a_\pm = [\mu_B g H \pm \sqrt{(\mu_B g H)^2 + E^2}]/E$ diagonalizes the potential terms (9) with eigenvalues (12a) to (12c). The basis order depends on the external magnetic field if we fix D and E. Note that still the original singlet state $|0\rangle$ remains unchanged. The two doublet states $|\pm1\rangle$ are rotated in the new basis.‖ To display the underlying physics in a clear way it is still convenient to use the singlet and doublet terminology, where the "doublet" now denotes the rotated former doublet states $|\pm1\rangle$, even if they are no longer degenerate.

2.3.2. Case $D > E$ In this section we discuss the configuration in which the single-ion anisotropy D is much stronger than the in-plane anisotropy E. The applied magnetic field is parallel as in (9). In this case the singlet $|2\rangle$ is initially energetically lower than the doublet, as per the left side of Figure 2. The components $|1\rangle$ and $|3\rangle$ further split due to the Zeeman effect. In accordance with the energy levels of the chemical potentials, we change the basis order as the magnetic field increases.

In the parameter region $H < \sqrt{D^2 - E^2}/(\mu_B g)$ we have basis order $|2\rangle, |1\rangle, |3\rangle$ with TBA driving terms

$$g_1 = -\frac{J}{v^2 + \frac{1}{4}} + D - \sqrt{(\mu_B g H)^2 + E^2},$$
$$g_2 = 2\sqrt{(\mu_B g H)^2 + E^2}. \tag{16}$$

Whereas for $H > \sqrt{D^2 - E^2}/(\mu_B g)$ we have basis order $|1\rangle, |2\rangle, |3\rangle$ with driving terms

$$g_1 = -\frac{J}{v^2 + \frac{1}{4}} - D + \sqrt{(\mu_B g H)^2 + E^2},$$
$$g_2 = D + \sqrt{(\mu_B g H)^2 + E^2}. \tag{17}$$

In this way we see that the parameters D, J, E and H either raise or lower the Fermi surfaces of colours $v^{(1)}$ and $v^{(2)}$. A gapped phase occurs if all sites are occupied by the

‖ Similar rotations have been considered by Huang and Affleck in a field theoretic study of the Haldane gap compound NENP [52].
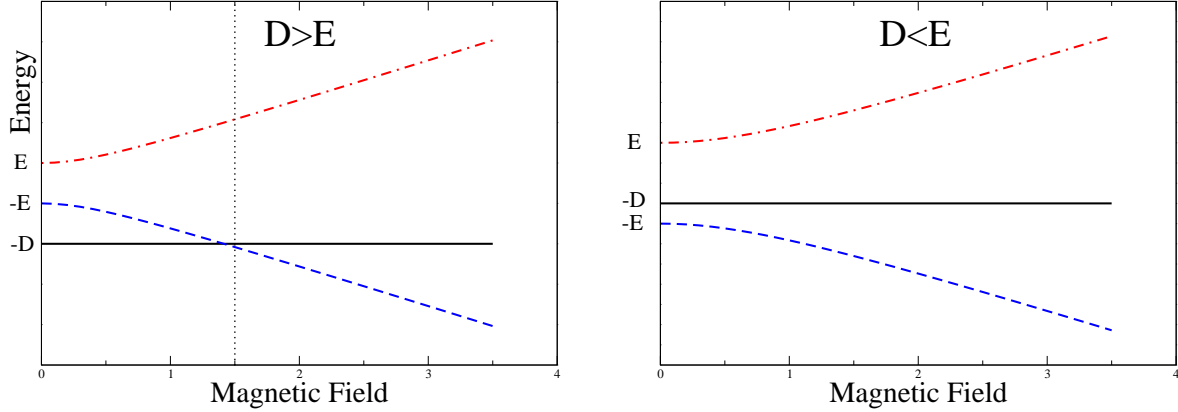
Figure 2. Chemical potential energy versus magnetic field for the parallel field case, equations (12a)-(12c), indicating level crossing. The left figure corresponds to equation (16) and the right figure corresponds to equation (17). The solid line (black) denotes the singlet $|2\rangle$ with energy μ_2, the dashed line (blue) denotes the doublet state $|1\rangle$ with energy μ_1 and the dot-dashed line (red) denotes the doublet state $|3\rangle$ with energy μ_3. In the left figure one level crossing occurs, marked by the dotted vertical line, while on the right side the basis order for the TBA analysis remains the same for all magnetic field. See text and also compare with Figure 4.

non-magnetic singlet in the ground state such that it takes a finite energy to excite the doublet. In the TBA picture this corresponds to the case where both *excitation bands* ϵ^1 and ϵ^2 are completely above the Fermi energy and therefore empty (see configuration D of Figure 1). From the TBA equations in the form (15) this can conveniently be calculated by finding for which (H, D, E) the gap conditions

$$\epsilon_1(v = 0, H, D, E) > 0 \quad \text{and} \quad \epsilon_2(v = 0, H, D, E) > 0 \tag{18}$$

hold. The restriction $v = 0$ could be used because it can be concluded from the form of (15) that the absolute minima of the dressed energies occur at the roots $v = 0$. From (15) and (18) it can be concluded that a gapped phase lies in the region

$$H < H_{c1} = \sqrt{(D - 4J)^2 - E^2}/\mu_B g. \tag{19}$$

Here H_{c1} is the critical field indicating a quantum phase transition from the nondegenerate singlet to the Luttinger liquid phase. The energy gap is given by

$$\Delta = D - 4J - \sqrt{(\mu_B g H)^2 + E^2}. \tag{20}$$

This gap is clearly weakened by the in-plane anisotropy as well as the magnetic field. The necessary condition for this gap to exist can be read off from (20) to be $D > 4J + E$. In the dressed energy picture this manifests itself by the point at which the lowest dressed energy $\epsilon^{(1)}$ just tips the Fermi energy $\epsilon_F = 0$ at its minimum, i.e. the transition D → C in Figure 1. Note that due to our basis-reordering procedure the dressed energies always satisfy $\epsilon^{(2)}(v) \geq \epsilon^{(1)}(v)$. Thus once $H > H_{c1}$ the component $|1\rangle$ with eigenvalue (12a) becomes involved in the ground state. At the critical point H_{c1} the phase transition is not

of Pokrovsky-Talapov type, due to the mixture of the former doublet states $|S^z = \pm 1\rangle$ in the state $|1\rangle$ with a field-dependent magnetic moment.

The magnetization increases as the magnetic field increases while more of component $|1\rangle$ becomes involved in the ground state. As usually defined in the TBA approach, the magnetization of an eigenstate of the system is

$$M(H) = \sum_{j=1}^{3} N_{|j\rangle} m_{|j\rangle}, \tag{21}$$

where the numbers $N_{|j\rangle}$ denote the total number of state $|j\rangle$ with magnetic moment

$$m_{|j\rangle} = -\frac{\partial}{\partial H} \mu_j(H). \tag{22}$$

Here μ_j are the eigenvalues of the chemical potentials. The occupation numbers $N_{|j\rangle}, j = 1, 2, 3$ are related to the Bethe quantum numbers M_1 and M_2 via (8), where M_1 and M_2 are given by

$$M_1 = \int \rho^{(1)}(v) \mathrm{d}v \qquad \text{and} \qquad M_2 = \int \rho^{(2)}(v) \mathrm{d}v. \tag{23}$$

From the driving terms in (17) we see that once the field increases beyond the second critical point

$$H_{c2} = \frac{\sqrt{(D+4J)^2 - E^2}}{\mu_B g}, \tag{24}$$

the ground state consists entirely of the $|1\rangle$ state. In this special case $M_1 = M_2 = 0$ holds, and therefore the reference state $|1\rangle$ becomes a true physical state with (normalized) magnetization

$$M_{H>H_{c2}}(H) = \frac{\mu_B g H}{\sqrt{E^2 + (\mu_B g H)^2}}. \tag{25}$$

We thus see that the magnetization in the pure $|1\rangle$ state gradually approaches the saturation magnetization $M_s = 1$ as the contribution to the magnetization from the original doublet state $|S^z = -1\rangle$ in the mixed state $|1\rangle$ tends to zero, whereas the state $|S^z = -1\rangle$ in the mixed state $|3\rangle$ becomes dominated. The probabilities of the components $|1\rangle$ and $|2\rangle$ are equal at the inflection point $H = \sqrt{D^2 - E^2}/\mu_B g$, where the magnetization $M_{\mathrm{IP}} = \frac{1}{2}\sqrt{1 - (E/D)^2}$. Actually, the magnetization between the critical fields can be obtained by numerically solving the TBA equations (15). This reduces to solving one integral equation instead of two coupled integral equations because the second level dressed energy is gapful in many cases (i.e. $\epsilon^{(2)}(v) > 0$). This numerically convenient case occurs when the general part B of Figure 1 reduces to part C. Indeed, in Figure 3, these novel phase transitions are observed in the magnetization derived from the TBA equations (15) and HTE free energy given by (44). As the spin-spin exchange interaction J decreases, the magnetization increases steeply in the vicinity of the critical point H_{c1}. If $J = 0$, i.e., for the case of independent spins, the critical points H_{c1} and H_{c2} merge into one point, at which a discontinuity in the magnetization of the ground state occurs. This is in agreement with the trivial exact solution of a single-spin system with energy levels (12a)-(12c).
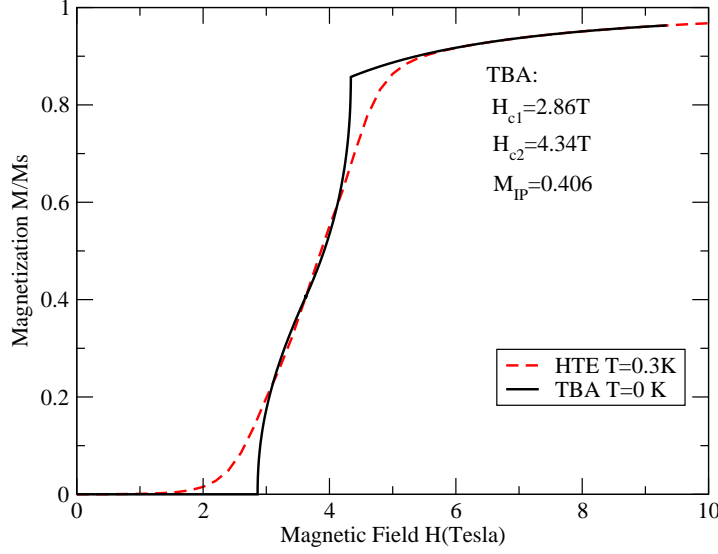
Figure 3. Magnetization versus magnetic field H in units of saturation magnetization for the Hamiltonian (2) with $J = 0.2$ K, $D = 6$ K, $E = 3.5$ K and $g = 2.0$ with parallel magnetic field. The solid and dashed lines show the magnetization derived from TBA and HTE at $T = 0$ and $T = 0.3$ K, respectively. The TBA magnetization curve indicates quantum phase transitions in the vicinity of H_{c1} and H_{c2} differing from the square root field-dependent critical behaviour. Their middle point has magnetization $M_{IP} \approx 0.406$ rather than $M_{IP} = 0.5$ in the case $E = 0$. Overall the TBA calculation is consistent with the HTE result.

2.3.3. Case $D \leq 4J + E$ If the single-ion anisotropy D lies in the region $E - 4J < D \leq E + 4J$, the energy levels of the chemical potentials (9) are as shown on the right side of Figure 2. The gapped phase does not exist in this regime. There are two competing components in the ground state, namely $|1\rangle$ and $|2\rangle$. In this case the basis order is $|1\rangle, |2\rangle, |3\rangle$ and the driving terms

$$g_1 = -\frac{J}{v^2 + \frac{1}{4}} - D + \sqrt{E^2 + (\mu_B g H)^2}$$
$$g_2 = D + \sqrt{E^2 + (\mu_B g H)^2} \tag{26}$$

apply throughout the whole range of the magnetic field. For very large magnetic field, i.e., $H > H_c$, where $H_c = \sqrt{(4J + D)^2 - E^2}/\mu_B g$, the ground state consists purely of the doublet state $|1\rangle$. Again, in the dressed energy picture, H_c is the point at which the first excitation band, here given by the singlet state $|2\rangle$, touches the Fermi energy $\epsilon_F = 0$ at its minimum, as per the transition D $\rightarrow$ C in Figure 1. To the right, i.e., for higher magnetic fields, both excitation bands $\epsilon^{(1)}$ and $\epsilon^{(2)}$ are completely gapped (part D of Figure 1). However, in the case $D < E - 4J$, all three states are involved in the ground state in a gapless phase.

2.3.4. Perpendicular magnetic field If a perpendicular magnetic field is applied to Hamiltonian (2), similar quantum phase transitions might occur as long as the in-plane anisotropy is much stronger than the planar anisotropy. Namely, if $E > D + 4J$, a gapped phase lies in the region $H < H_{c1}$, where the critical field

$$H_{c1} = \frac{\sqrt{2(E - 2J)(E - 4J - D)}}{\mu_B g}.$$

(27)

The magnetization increases almost linearly as the magnetic field increases above H_{c1}. A quantum phase transition occurs at the critical point H_{c2}, where

$$H_{c2} = \frac{\sqrt{2(E + 2J)(E + 4J - D)}}{\mu_B g}.$$

(28)

The magnetization tends to saturation as the field becomes stronger than H_{c2}. However, if $E < D + 4J$, there is no gapped phase even in the absence of the magnetic field.

2.3.5. Special case 1: Absence of in-plane anisotropy ($E = 0$) Now consider Hamiltonian (2) with chemical potentials (9) for the special case $E = 0$. This will be used to analyze the compound NENC in section 3.2, which is believed to have negligible in-plane anisotropy. The fundamental basis, $|1\rangle = |+1\rangle$, $|2\rangle = |0\rangle$ and $|3\rangle = |-1\rangle$, diagonalizes the chemical potential terms with eigenvalues

$$\mu_1 = -\mu_B g H,$$
$$\mu_2 = -D,$$
$$\mu_3 = \mu_B g H.$$

(29)

Taking $E = 0$ in the driving terms in the different regions, we find that the ground state in the zero temperature limit has a gap if the single-ion anisotropy $D > 4J$. The singlet $|2\rangle$ ground state is separated from the lowest spin excitation by an energy gap $\Delta = D - 4J$. This energy gap is decreased by the external magnetic field H. The pure singlet ground state breaks down at the critical point $H_{c1} = (D - 4J)/\mu_B g_s$. The magnetization almost linearly increases with increasing magnetic field due to the magnon excitation. We discuss this further via the HTE approach in section 2.4. The ground state is fully polarized once the magnetic field increases beyond the second critical point $H_{c2} = (D + 4J)/(\mu_B g)$, i.e., in the $M = M_s$ saturation plateau region. A gapped phase can only exist for anisotropy values satisfying the 'strong anisotropy' condition $D > 4J$. As shown in [22] the magnetization in the vicinity of the critical fields H_{c1} and H_{c2} depends on the square root of the field, indicating a Pokrovsky-Talapov type transition. In this regime, the anisotropy effects overwhelm the biquadratic spin-spin interaction contribution and open a gapped phase in the ground state.

2.3.6. Special case 2: Trivalent orbital splitting Here we consider a further specialization of the previous case (9) which can be mapped onto it via the identification

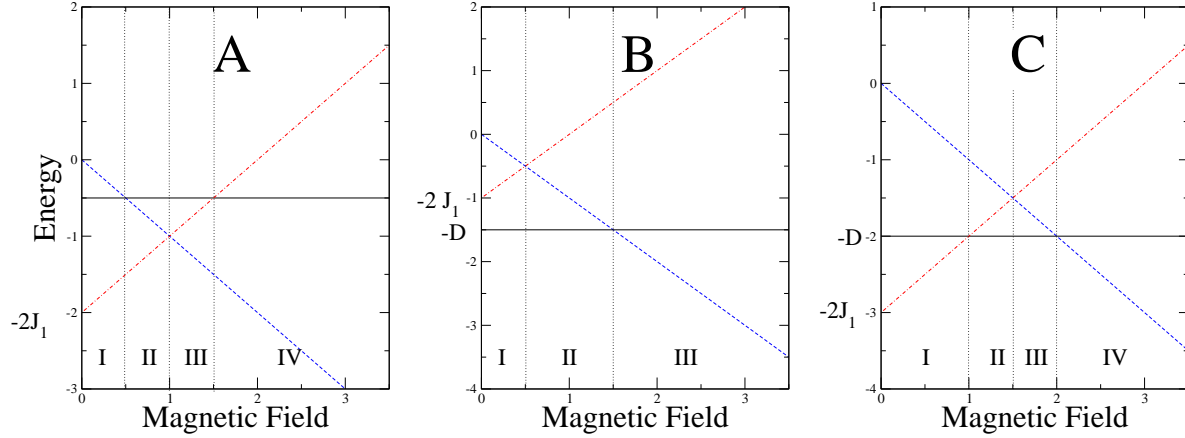$$(H', D', E') = (H + 2J_1, D - 2J_1, 0),$$

(30)

Figure 4. Energy levels versus magnetic field for eigenvalues (32) of the operator (31). The solid line (black) denotes the singlet $|0\rangle$, the dashed line (blue) denotes the doublet $|+1\rangle$ and the dash-dotted line (red) denotes the other doublet state $|-1\rangle$. The vertical dotted lines and the roman numerals mark the change of basis order in the TBA analysis (see text). Shown are the three typical choices of coupling constants. For their connection to energy gaps and magnetization plateau see the text and also Figure 5 and Figure 6.

where the primed constants are those apearing in the general model (9). We have not found an experimental spin-compound realization of this particular Hamiltonian so far. Nevertheless, we give the TBA analysis here, as it has new and interesting physics in its own right, as it incorporates a physical mechanism to open more unusal gapped states and magnetization plateaux.

If we consider the orbital degrees in the Hamiltonian, trivalent orbital splitting, as well as interatomic effects, may result in an alignment of the internal magnetic field to prefer one component of the spin doublet. To represent this physical effect we add a projection operator to the chemical potentials, so that

$$\mathcal{H}_{i,\text{chem.pot}} = D \sum_{j=1}^{L}(S_j^z)^2 - J_1 \sum_{j=1}^{L} S_j^z(S_j^z - 1) - \mu_B gH \sum_{j=1}^{L} S_j^z. \tag{31}$$

This additional term gives rise to a rich phase diagram by shifting the energy levels, as seen in the difference between Figure 2 and Figure 4. The on-site energy eigenvalues are now given by

$$\begin{aligned}
\mu_{|+1\rangle} &= -\mu_B gH, \\
\mu_{|0\rangle} &= -D, \\
\mu_{|-1\rangle} &= \mu_B gH - 2J_1,
\end{aligned} \tag{32}$$

where the fundamental basis, $|1\rangle = |+1\rangle$, $|2\rangle = |0\rangle$ and $|3\rangle = |-1\rangle$, diagonalizes the chemical potential term.

In general, the magnetization curves for this case can have up to 3 gapped phases, as shown in part (B) of Figure 5. Note that all magnetization plots in this figure have

been obtained by the HTE method for relatively low temperatures and are therefore only similar to the zero-temperature magnetization. Numerical solution of the TBA equations gives slightly 'sharper' contours. Variations in the parameter set (J, J_1, D) can open or close the different gapped phases. After calculating the whole phase diagram via the TBA, analogously as done in Refs [22, 23, 24], we show the physically interesting choices of coupling constants, corresponding to the four pictures in Figure 5. Here we have restricted our analysis to small exchange coupling values $J < D/4$. We now consider the model in the region $J_1 < D < J_1 + 4J$, corresponding to configuration A of Figure 4. Proceeding with the basis orders

$$(|3\rangle, |2\rangle, |1\rangle) \rightarrow (|3\rangle, |1\rangle, |2\rangle) \rightarrow (|1\rangle, |3\rangle, |2\rangle) \rightarrow (|1\rangle, |2\rangle, |3\rangle), \tag{33}$$

we analyze the ground state properties from the TBA equations (15) with different driving terms. The technique is similar to the previous section and we omit the details of the driving terms. It is interesting that a degenerate gapped phase starts from zero field. The ground state consists of the doublet state $|3\rangle$ with spin $S^z = -1$. This state is separated from the lowest magnon excitation by the energy gap

$$\Delta = 2J_1 - D - 4J. \tag{34}$$

The magnetic field lifts the energy level of the state $|3\rangle$ and the gap vanishes when the magnetic field exceeds the first critical field

$$H > H_{c1} = \frac{2J_1 - D - 4J}{\mu_B g}. \tag{35}$$

The singlet state and the other doublet state $|1\rangle$ subsequently become involved in the ground state. Thus the magnetization increases almost linearly as the magnetic field increases. It is worth noting that the singlet state is suppressed by the strong potential J_1. The ground state is fully-polarized beyond the second critical magnetic field

$$H > H_{c2} = \frac{D + 4J}{\mu_B g}. \tag{36}$$

This phase diagram is shown in part (A) of Figure 5.

In the region $J_1 + 4J < D < 2J_1 - 4J$, we find the situation as depicted in configuration (C) of Figure 4, where the model exhibits three different gapped phases due to existence of a strong single-ion anisotropy. Here the basis orders become

$$(|3\rangle, |2\rangle, |1\rangle) \rightarrow (|2\rangle, |3\rangle, |1\rangle) \rightarrow (|2\rangle, |1\rangle, |3\rangle) \rightarrow (|1\rangle, |2\rangle, |3\rangle). \tag{37}$$

The plateau with total spin $S^z = -1$ starts at zero field. The energy level of this state is increased by the external magnetic field, so that the spin singlet completely displaces the doublet from the ground state when the field exceeds $H > H_{c2}$. This field-induced nonmagnetic mid-plateau opens with the anisotropy parameter D. However, it can be closed for certain large values of J. The critical fields predicted by the TBA analysis are given by

$$H_{c1} = \frac{2J_1 - D - 4J}{\mu_B g}, \qquad H_{c2} = \frac{2J_1 - D + 4J}{\mu_B g},$$

$$(38)$$

$$H_{c3} = \frac{D - 4J}{\mu_B g}, \qquad\qquad H_{c4} = \frac{D + 4J}{\mu_B g}.$$

Further physical interpretation of these critical fields is given in section 2.4 via the HTE approach (see part (B) in Figure 5). If the single-iron anisotropy becomes larger, such that $2J_1 - 4J < D < 2J_1 + 4J$, the gapped spin $S^z = -1$ state is weakened by the singlet, whose energy level decreases. Thus the doublet magnetic ground state is gapless as long as the field is below H_{c2}. In this case the mid-plateau can still survive (see part (C) in Figure 5). Except for the absence of the first critical field H_{c1}, the other critical fields in (38) remain valid for this case. However, if D is large enough a nondegenerate singlet state can start from zero field. This scenario is depicted in part (B) of Figure 4. In this case, the anisotropy J_1 is suppressed. The critical fields are the same as in section 2.3.5.

2.4. HTE analysis: properties at high temperatures

We begin by briefly reviewing the idea of the HTE method, which we use to predict physical properties of the spin chain compounds in the next section.

The Bethe Ansatz as described in section 2.1 is based on a row-to-row transfer matrix, which has the disadvantage that its largest eigenvalue may be degenerate. Moreover, the TBA equations suffer from infinitely many nonlinear integral equations (NLIE). On the other hand, the Quantum Transfer Matrix (QTM) [16] considers the transfer matrix on a square lattice with an inhomogeneity parameter value $u_N = -\beta J/N$ (N is the Trotter number). The largest eigenvalue is non-degenerate [17] and the free energy is determined only by the largest eigenvalue of the QTM. The advantage of the QTM formalism is that the problem of deriving the largest eigenvalue reduces to solving finitely many NLIE. The nested Bethe equations take a slightly different form than in the row-to-row case.

For the model at hand, the eigenvalue of the QTM is given by

$$
\begin{aligned}
T_1^{(1)}\left(v, \left\{v_i^{(a)}\right\}\right) = {}& e^{-\beta\mu_1}\ \phi_-(v - i)\phi_+(v)\frac{Q_1(v + \frac{1}{2}i)}{Q_1(v - \frac{1}{2}i)} \\
& + e^{-\beta\mu_2}\ \phi_-(v)\phi_+(v)\quad \frac{Q_1(v - \frac{3}{2}i)}{Q_1(v - \frac{1}{2}i)}\ \frac{Q_2(v)}{Q_2(v - i)} \\
& + e^{-\beta\mu_3}\ \phi_-(v)\phi_+(v + i)\frac{Q_2(v - 2i)}{Q_2(v - i)}.
\end{aligned}
\tag{39}
$$

Here we follow notation from Ref. [15], with $\phi_\pm(v) = (v \pm iu_N)^{\frac{N}{2}}$ and $Q_a(v) = \prod_{i=1}^{M^{(a)}}(v - v_i^{(a)})$ for $a = 1, 2$. The Bethe roots $v_i^{(a)}$ are solutions of the QTM Bethe equations

$$
\left(\frac{v_j^{(1)} - iu_N + \frac{1}{2}i}{v_j^{(1)} - iu_N - \frac{1}{2}i}\right)^{\frac{N}{2}} = e^{-\frac{\mu_1 - \mu_2}{T}} \prod_{\substack{l=1 \\ l \neq j}}^{M_1} \frac{v_j^{(1)} - v_l^{(1)} + i}{v_j^{(1)} - v_l^{(1)} - i} \prod_{l=1}^{M_2} \frac{v_j^{(1)} - v_l^{(2)} - \frac{1}{2}i}{v_j^{(1)} - v_l^{(2)} + \frac{1}{2}i},
$$

$$\left(\frac{v_k^{(2)} + \mathrm{i}u_N + 2\mathrm{i}}{v_k^{(2)} + \mathrm{i}u_N + \mathrm{i}}\right)^{\frac{N}{2}} = \mathrm{e}^{-\frac{\mu_2 - \mu_3}{T}} \prod_{i=1}^{M_1} \frac{v_k^{(2)} - v_i^{(1)} - \frac{1}{2}\mathrm{i}}{v_k^{(2)} - v_i^{(1)} + \frac{1}{2}\mathrm{i}} \prod_{\substack{l=1 \\ l \neq k}}^{M_2} \frac{v_k^{(2)} - v_l^{(2)} + \mathrm{i}}{v_k^{(2)} - v_l^{(2)} - \mathrm{i}}. \quad (40)$$

In the above $j = 1, \ldots, M_1$ and $k = 1, \ldots, M_2$.

The eigenvalue $T_1^{(1)}(v)$ is embedded in a family of eigenvalues $T_m^{(a)}(v)$ for related models via the fusion hierarchy [18]. These eigenvalues are connected to each other by the functional relation (42) known as the T-system. The indices of $T_m^{(a)}$ denote that the auxiliary space has fusion type (a, m). It carries the m-fold symmetric tensor of the a-th fundamental representation of the $su(3)$ Lie algebra. The relations can be conveniently denoted graphically by Young tableaux, where the simple case only deals with rectangular shaped blocks (see Refs [15] and [18]). The fused eigenvalues are explicitly given by

$$T_m^{(a)} = \sum_{d_{j,k}} \prod_{j=1}^{a} \prod_{k=1}^{m} z(d_{j,k}; v - \tfrac{1}{2}\mathrm{i}(a - m - 2j + 2k)), \quad (41)$$

where the summation is taken over the "Young tableaux" parameter $d_{j,k} \in \{1, 2, 3\}$ such that $d_{j,k} < d_{j+1,k}$ and $d_{j,k} \leq d_{j,k+1}$, which form an $a \times m$ rectangular tableaux. After a renormalization the functional relation takes the simple form

$$\tilde{T}_m^{(a)}(v + \tfrac{1}{2}\mathrm{i})\tilde{T}_m^{(a)}(v - \tfrac{1}{2}\mathrm{i}) = \tilde{T}_{m+1}^{(a)}(v)\tilde{T}_{m-1}^{(a)}(v) + \tilde{T}_m^{(a-1)}(v)\tilde{T}_m^{(a+1)}(v). \quad (42)$$

in the normalized functions $\tilde{T}_m^{(a)}$ [15].

By exploiting knowledge of analyticity properties, and numerically backed assumptions about the largest eigenvalue and the locations of its zeroes, this T-system can be transformed into a set of coupled NLIE. These NLIE had first been discussed for the spin-$\frac{1}{2}$ chain ($su(2)$-XXX model) in [14]. The general $su(n)$ case was derived by Tsuboi [15] in full detail. For the integrable spin-1 chain ($su(3)$-case) considered here the coupled NLIE are

$$T_1^{(0)}(v) = \exp\left(\frac{J}{T}\frac{1}{v^2 + \frac{1}{4}}\right),$$

$$T_1^{(1)}(v) = Q_1^{(1)} + \oint_{c_1^1} \frac{\mathrm{d}y}{2\pi\mathrm{i}} \frac{T_1^{(0)}(y+\beta_1^{(1)}-\frac{1}{2}\mathrm{i})T_1^{(2)}(y+\beta_1^{(1)}-\frac{1}{2}\mathrm{i})}{(v-y-\beta_1^{(1)})T_1^{(1)}(y+\beta_1^{(1)}-\mathrm{i})} + \oint_{c_2^1} \left\{ \begin{matrix} \mathrm{i} \to -\mathrm{i} \\ \beta_1^{(1)} \to -\beta_1^{(1)} \end{matrix} \right\},$$

$$T_1^{(2)}(v) = Q_2^{(1)} + \oint_{c_1^2} \frac{\mathrm{d}y}{2\pi\mathrm{i}} \frac{T_1^{(1)}(y+\beta_1^{(2)}-\frac{1}{2}\mathrm{i})T_1^{(3)}(y+\beta_1^{(2)}-\frac{1}{2}\mathrm{i})}{(v-y-\beta_1^{(1)})T_1^{(2)}(y+\beta_1^{(2)}-\mathrm{i})} + \oint_{c_2^2} \left\{ \begin{matrix} \mathrm{i} \to -\mathrm{i} \\ \beta_1^{(2)} \to -\beta_1^{(2)} \end{matrix} \right\},$$

$$T_1^{(3)}(v) = \exp\left((\mu_1 + \mu_2 + \mu_3)/T\right) = \mathrm{const}. \quad (43)$$

Here the contours c_i^j are counterclockwise closed loops around zero, omitting certain special points [15].

The first remarkable property of these new NLIE's is that there are only finitely many of them, as the n-th eigenvalue in this hierarchy is constant in terms of the spectral parameter v, in contrast to the finite temperature TBA considered in section 2.3. The second useful property is the fact that these NLIE's can be solved by an expansion in the small parameter J/T, for which the coefficients can be obtained *recursively*. This

distinguishes the HTE method from other NLIE approaches, e.g., Ref. [17], where the NLIE has to be solved numerically.

The result for the free energy of the $su(3)$ case (already stated in Ref. [15]) is

$$- \frac{1}{T} f(T, H) = \ln Q_1^{(1)} + C_{1,0}^1 \left(\frac{J}{T} \right) + C_{2,0}^1 \left(\frac{J}{T} \right)^2 + C_{3,0}^1 \left(\frac{J}{T} \right)^3 + \cdots \quad (44)$$

where the first few coefficients are given by

$$c_{1,0}^{(1)} = 2 \frac{Q_1^{(2)}}{Q_1^{(1)\,2}},$$

$$c_{2,0}^{(1)} = 3 \frac{Q_1^{(2)}}{Q_1^{(1)\,2}} - 6 \frac{Q_1^{(2)\,2}}{Q_1^{(1)\,4}} + 3 \frac{Q_1^{(3)}}{Q_1^{(1)\,3}},$$

$$c_{3,0}^{(1)} = \frac{10}{3} \frac{Q_1^{(2)}}{Q_1^{(1)\,2}} - 18 \frac{Q_1^{(2)\,2}}{Q_1^{(1)\,4}} + \frac{80}{3} \frac{Q_1^{(2)\,3}}{Q_1^{(1)\,6}} + 8 \frac{Q_1^{(3)}}{Q_1^{(1)\,3}} - 24 \frac{Q_1^{(2)} Q_1^{(3)}}{Q_1^{(1)\,5}},$$

in terms of the su(3) Q-system

$$\begin{aligned} Q_1^{(1)} &= e^{-\beta \mu_1} + e^{-\beta \mu_2} + e^{-\beta \mu_3}, \\ Q_1^{(2)} &= e^{-\beta \mu_1 - \beta \mu_2} + e^{-\beta \mu_1 - \beta \mu_3} + e^{-\beta \mu_2 - \beta \mu_3}, \\ Q_1^{(3)} &= e^{-\beta \mu_1 - \beta \mu_2 - \beta \mu_3}. \end{aligned} \quad (45)$$

We find that considering only terms up to third order is sufficient for the analysis of real compounds. This is different from other types of high temperature series expansion [60]. The HTE coefficients are functions of the chemical potentials μ_i, i.e., they depend on the external parameters such as the coupling strength and magnetic field. The thermodynamic behaviour can be directly obtained from the free energy (44) via the standard relations

$$M = - \left(\frac{\partial}{\partial H} f(T, H) \right)_T, \quad \chi = - \left(\frac{\partial^2}{\partial H^2} f(T, H) \right)_T, \quad C = -T \left(\frac{\partial^2}{\partial T^2} f(T, H) \right)_H, \quad (46)$$

for the magnetization, magnetic susceptibility and magnetic specific heat. We apply these results to several spin compounds in section 3. Now the *small parameter* of the expansion is J/T, i.e., the expansion is expected to work well for spin chain materials with relatively weak intrachain coupling.

Before proceding, we note that in the above theory, the largest QTM eigenvalue is only fixed up to a (positive) constant. From the derivation of the HTE it can be seen that the free energy expansion

$$f_{HTE}(T, H) = c_0 + c_1 \frac{J}{T} + c_2 \left(\frac{J}{T} \right)^2 + c_3 \left(\frac{J}{T} \right)^3 + \dots \quad (47)$$

is only fixed up to a multiplicative constant, i.e.

$$\begin{aligned} f_{\text{phys.units}} &= \gamma_{\text{conv.}} f_{HTE}(T, H) \\ &= \gamma_{\text{conv.}} \left[c_0 + c_1 \frac{J}{T} + c_2 \left(\frac{J}{T} \right)^2 + c_3 \left(\frac{J}{T} \right)^3 + \dots \right]. \end{aligned} \quad (48)$$

Physically, this amounts to the fact that in the theory we don't specify the unit of energy, i.e. there is no analogue of a 'characteristic length'. Mathematically it can be traced back to the multiplicativity of the underlying R-matrix of the integrable model. In practice this factor depends on the choice of units for the physical free energy.

Another remaining problem is the apparent widespread use of non-standard non-SI units in the experimental community for measurements on real compounds which sometimes even depend on compound specifics such as molecular mass. In eq.(48) the unknown constant $\gamma_{\mathrm{conv.}}$ is a prefactor, i.e., the same in all orders of the expansion. The expansion is generated for interacting spins from the Bethe Ansatz. For zero order, the non-interacting case $J = 0$, it reduces to the exact trivial solution for L independent spins (here, e.g., for a 2-state spin-1/2 system):

$$f_{0-\mathrm{th\,order}} = \gamma_{\mathrm{conv.}} c_0 \equiv -k_B T \ln \left(e^{\frac{\mu_1}{k_B T}} + e^{\frac{\mu_2}{k_B T}} \right). \tag{49}$$

The second equality only holds for the special point $J = 0$, but as $\gamma_{\mathrm{conv.}}$ is a constant it can be extended in eq.(48) to all $J > 0$.

Once the free energy is thus known in SI units, say [J], it is trivial to obtain all other properties dervied from it in SI units via

$$M_{\mathrm{phys.units}} = -\frac{\partial}{\partial H} f_{\mathrm{phys.units}}. \tag{50}$$

The important point here is that HTE can make predictions in physical units, even if the original T-system is only valid up to a constant. Thus all conversion factors can in theory be calculated using the additional information from the non-interacting spin system. In addition, for real compounds the parameters D, E and J are given in Kelvin. For convenience, we omit in this paper the Boltzmann constant k_B in the conventional notations D/k_B, E/k_B, J/k_B.

We found different spin-1 compounds have the same conversion factor for the susceptibility. In this way if we normalise the magnetic properties, such as the magnetization (M/M_s), the conversion constant does not play any role in fitting the experimental data. On the other hand, the conversion constant for the specific heat is material dependent due to the choice of units in a given experiment. For convenience we state these factors in the relevant figure caption each time they are used.

2.4.1. Special case: Trivalent orbital splitting In this section we consider the special Hamiltonian (31), already studied via the TBA method. Diagonalizing the Hamiltonian we find the chemical potential terms (32)

$$\begin{aligned} \mu_1 &= -\mu_B g H, \\ \mu_2 &= -D, \\ \mu_3 &= \mu_B g H - 2J_1. \end{aligned} \tag{51}$$

We plot the magnetization versus magnetic field and the susceptibility versus temperature for different configurations in Figure 5 and Figure 6, corresponding to the parameter sets found in the TBA analysis in section 2.3. Comparing the results
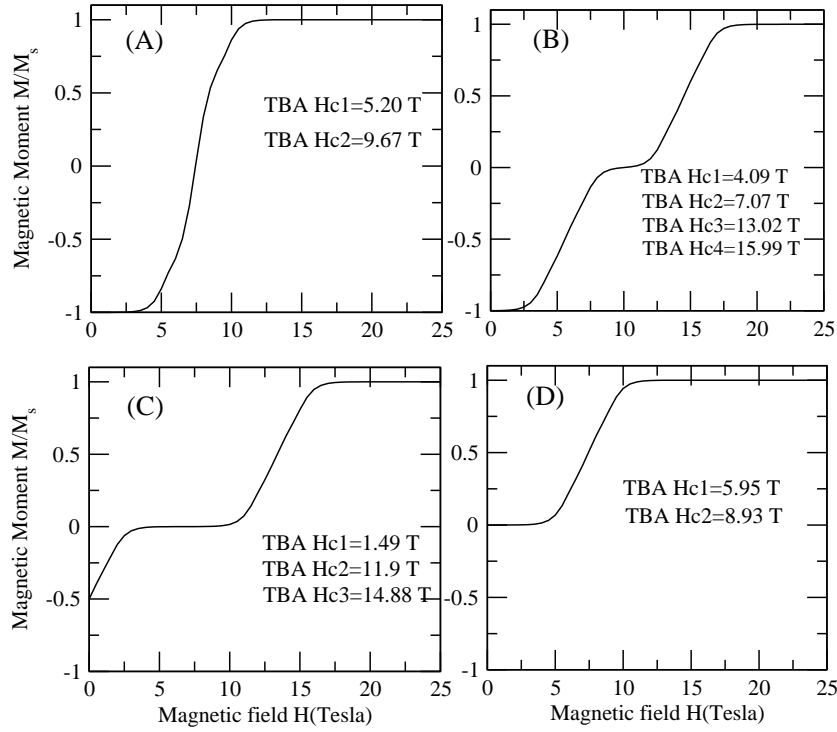
Figure 5. Magnetization versus magnetic field at $T = 0.8$K for the Hamiltonian (2) evaluated directly from the HTE. The structure constants are (A) $D = 11$K, $J_1 = 10$K and $J = 0.5$K; (B) $D = 19.5$K, $J_1 = 13.5$K and $J = 0.5$K; (C) $D = 18$K, $J_1 = 9$K and $J = 0.5$K; (D) $D = 11$K, $J_1 = 0$K and $J = 0.5$K. In each case $\mu_B = 0.672$K/T and $g = 2.0$. The critical fields estimated from the magnetization curve coincide with the TBA results.

of both approaches (see Figure 5 for numerical TBA values) we find that the critical fields obtained by the TBA coincide well with the values from the HTE free energy (44), even at relatively low temperatures. For case (A) in Figure 5 and Figure 6, where $J_1 < D < J_1 + 4J$, a field-induced gap exists in the lowest magnon excitation. The ground state lies in a magnetic doublet state with an energy gap. Note the typical rounded peak in the susceptibility for the antiferromagnetic gapped spin chain. For case (B), further enhancement of the anisotropy D into the region $J_1 + 4J < D < 2J_1 - 4J$ opens a non-magnetic singlet mid-plateau. This leads to a spin-Peierls-like quantum phase transition. The magnetic ground state is gapped, as before. If the single-ion anisotropy D is large enough, the gapped ground state is weakened by the singlet potential. If $2J_1 - 4J < D < 2J_1 + 4J$, the ground state shifts into a gapless phase, as shown in case (C). The round peak in the susceptibility curve, indicating an energy gap, now gets replaced by a steep increase for temperatures close to zero, indicating a gapless phase. In this case, the mid-plateau remains open if the anisotropy is large enough, i.e., if $2J_1 - 4J < D < 2J_1 + 4J$. The most common gapped phase is found in
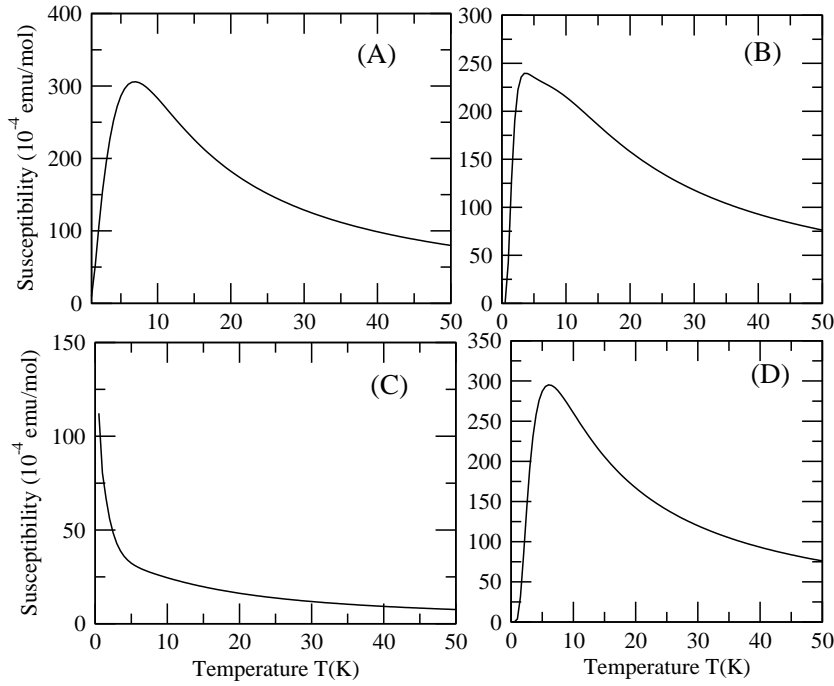
Figure 6. Susceptibility versus temperature at $H = 0$ T. The numerical values are the same as in the previous figure. The susceptibility curves in (A), (B) and (D) indicate the existence of energy gaps, while no significant gap can be observed in (C).

case (D), where $J_1 = 0$ and the anisotropy is large, $D > 4J$. A non-magnetic singlet occupies the whole ground state as long as the energy gap $\Delta = D - 4J$ remains closed by the external magnetic field. We are now ready to move onto the direct comparison with experimental results.

3. Examination of real compounds

The compounds to be examined via the integrable spin-1 model (2) are listed in Table 1. We summarize the coupling constants obtained from the Heisenberg chain (HC) and our model (HTE and TBA). We shall see below that the thermal and magnetic properties derived from the HTE method are in excellent agreement with the experimental results.

3.1. Nickel salts

Certain Nickel salts can be described by the spin-1 Hamiltonian (2) with chemical potentials (9) and (10) with $E = 0$. The chemical potential terms are explicitly given in (29) for the parallel case (9), i.e.

$$\mu_1 = -\mu_B g H,$$

Compound	HC J	HC D	HC E	HTE J	HTE D	HTE E	TBAH_{c1}	TBAH_{c2}
NiSnCl	0.02K	0.64K	0K	0.02K	0.64K	0K	0.38 T	0.49 T
NENC	0.65K	6.15K	0.7K	0.17K	6.4K	0K	3.8 T	4.7 T
NBYC	0.2K	2.55K	1.5K	0.35K	2.62K	1.49K	N/A	2.7 T
NDPK	0.96K	5.0K	2.8K	0.55K	5.15K	2.55K	1.0 T	4.66T

Table 1. Estimates for the exchange coupling J and anisotropy constants D and E for some real compounds. Here HC denotes the values obtained from numerical fits for the spin-1 Heisenberg chain [46, 47, 48, 49] and HTE denotes the values obtained using the integrable spin-1 model and the HTE method. Also shown are the corresponding TBA estimates for the critical magnetic fields.

$$\mu_2 = -D,$$
$$\mu_3 = \mu_B g H,$$

and for the perpendicular magnetic field case (10),

$$\mu_1 = -\frac{1}{2}(D + \sqrt{D^2 + (2\mu_B g H)^2}),$$
$$\mu_2 = 0,$$
$$\mu_3 = -\frac{1}{2}(D - \sqrt{D^2 + (2\mu_B g H)^2}).$$

A large zero-field splitting effect was identified in some nickel salts, such as NiSnCl$_6 \cdot$ 6H$_2$O (abbreviated as NiSnCl) [43], [Ni(C$_5$H$_5$NO)$_6$](ClO$_4$)$_2$ [44] and Ni(NO$_3$)$_2 \cdot$ 6H$_2$O [45]. Here the Ni^{2+} ion causes a large splitting between the singlet and doublet in the spin triplet in an axially distorted crystalline field. For $D > 0$ and no magnetic field, the triplet is split into a lower singlet and an excited doublet. An early theoretical prediction for this kind of compound was done as a first order approximation via Van Vleck's equation [50]. In this treatment the exchange interaction is neglected in first order for the specific heat, magnetization and susceptibility. An effective field was introduced for the magnetization and susceptibility to fit the experimental data. In section 2.3, we have shown that large anisotropies D may drive the antiferromagnetic spin chain into a gapped phase, which is significantly different from the valence-bond-solid ground state. Examining the magnetic properties of the salt NiSnCl$_6 \cdot$ 6H$_2$O [43] via the HTE method, we find that the measurements are best fitted by a model with zero-field splitting $D \approx 0.64K$ and a much weaker spin exchange interaction $J \approx 0.02K$. Actually even the zero order HTE with free energy (44) gives a good analytic result for this compound [43]. As expected, the zero order term of the HTE free energy is just the result for L non-interacting identical spins with three energy levels μ_1, μ_2 and μ_3, i.e.

$$f(H,T)_{\text{free spin}} = -T \ln(e^{-\mu_1/T} + e^{-\mu_2/T} + e^{-\mu_3/T}). \tag{52}$$

Comparing this with the zero order HTE term in (44), i.e., with $\ln Q_1^{(1)}$, we see that (52) is identical to the first term in the Q-System (44).

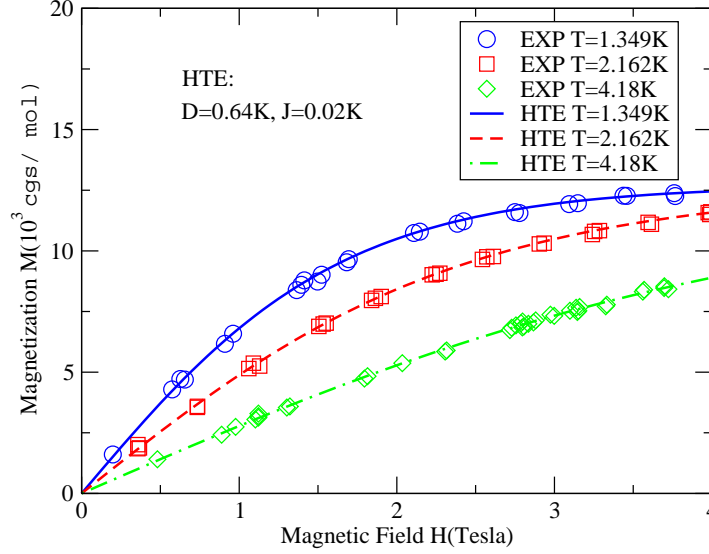In Figure 7 we compare the magnetization obtained from the theoretical free energy

Figure 7. Comparison between theory and experiment [43] for the magnetization versus magnetic field of the compound $NiSnCl_6 \cdot 6H_2O$. The magnetic field is parallel to the trigonal axis. A parameter fit suggests the coupling constants $D = 0.64$ K, $J = 0.02$ K, $g_\parallel = 2.22$ with $\mu_B = 0.672$ K/T. The conversion constant is $M_{HTE} \approx 8.5 M_{EXP}$ (10^3 cgs/mol). The agreement between the theoretical curves derived here from the HTE approach and the experimental data suggests that the compound might exhibit zero-field splitting with much stronger splitting strength D than the spin exchange interaction J.

expression (44) with parameters

$$D \approx 0.64K, \qquad J \approx 0.02K, \qquad g_\parallel = 2.22,$$

at temperatures $T = 1.349K$, $T = 2.162K$ and $T = 4.18K$ with the experimental data for $NiSnCl_6 \cdot 6H_2O$. They show excellent agreement. The experimental curves are for the case of the external magnetic field parallel to the trigonal axis given by the crystal sample. The magnetic properties are anisotropic with respect to the external field direction. From our TBA analysis, at zero temperature, the energy gap is $\Delta \approx 0.55$ K for this salt. At very low temperatures the system mainly occupies the non-degenerate singlet ground state if the magnetic field is less than the critical field H_{c1}. The length of the antiferromagnetic correlations is finite. For higher temperatures $T > D$, the singlet ground state no longer dominates, with excitations caused by spin flips.

In some experiments the samples are not of macroscopic crystal size, thus it is not possible to align the material parallel to an external field direction. In such 'powder' samples we assume an isotropic distribution and use the heuristic formula (see p121 in Ref. [50])

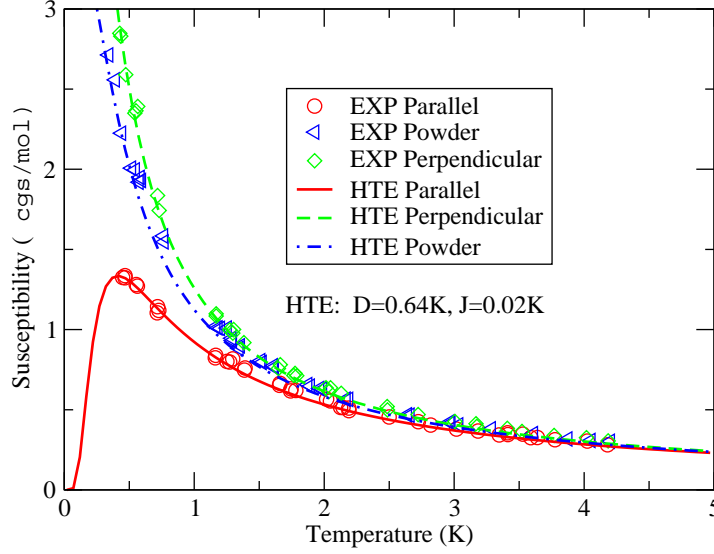$$\chi_{\text{powder}} \approx \tfrac{1}{3}\chi_\parallel + \tfrac{2}{3}\chi_\perp, \tag{53}$$

Figure 8. Comparison between theory and experiment [43] for the susceptibility versus temperature of the compound $NiSnCl_6 \cdot 6H_2O$. A parameter fit suggests the coupling constants $D = 0.64$ K, $J = 0.02$ K, $g_\parallel = 2.22$ and $g_\perp = 2.20$ with $\mu_B = 0.672$ K/T. The conversion constant is $\chi_{HTE} \approx 0.8123\chi_{EXP}$ (cgs/mol). The agreement between the HTE curve and the experimental data confirm that the compound $NiSnCl_6 \cdot 6H_2O$ exhibits zero-field splitting with a larger strength than the spin exchange interaction.

where $\chi_\parallel$ and $\chi_\perp$ refer to the model Hamiltonian (2) with respective on-site interactions (9) and (10). This simple ansatz describes the experimental data quite well, as can be seen in Figure 8 where all three susceptibilities – parallel, perpendicular and powder – have been measured for this compound. The temperature dependence of the magnetic susceptibility for powdered samples and the HTE predictions using the above averaging formula are given in Figure 8. The typical rounded peak in the low magnetic field susceptibility curve, characteristic of low-dimensional antiferromagnets, are predicted to occur around 0.41 K from the HTE relation $\chi_\parallel = -\frac{\partial^2}{\partial H^2} f_{HTE}(T, H)$ for the parallel magnetic field. Using the same physical model, i.e., with the same parameters as for the specific heat comparison, we find that the susceptibility $\chi_\parallel$ is in good agreement with the experimental curve. If the magnetic field is perpendicular to the trigonal axis (respectively along the x or y axis), the susceptibility is given by $\chi_\perp = -\frac{\partial^2}{\partial H^2} f_{HTE}(T, H)$ with the perpendicular magnetic field chemical potentials. We see that our theoretical curve, depicted by the dashed line in Figure 8, gives a good fit to the experimental susceptibility curve with perpendicular field. It also suggests the same parameter constants, except $g_\perp = 2.20$.

In Figure 9 the specific heat curve for $H = 0$ T shows that the HTE result agrees with the experimental data [43] in the available temperature region. Note that we do not change the coupling constants to get a best fit for each physical property. Rather we assign fixed coupling constants to each compound and thus truly predict
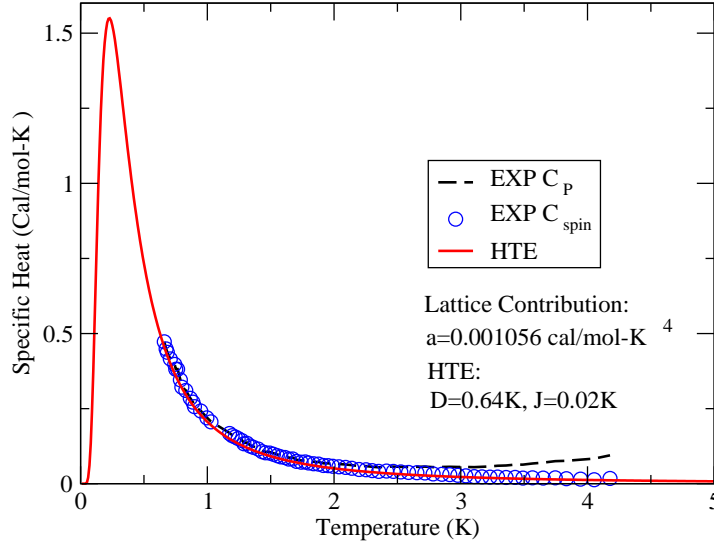
Figure 9. Comparison between theory and experiment [43] for the magnetic specific heat versus temperature of the compound $NiSnCl_6 \cdot 6H_2O$. A parameter fit suggests the coupling constants $D = 0.64$ K, $J = 0.02$ K, $g = 2.2$ with $\mu_B = 0.672$ K/T. The conversion constant is $C_{HTE} \approx 1.920 C_{EXP} (cal/mol - K) \approx 8 C_{EXP}$ (J/mol-K). The dashed line represents the experimental measured values C_P including the lattice contribution. The circle curve is the corrected magnetic specific heat without a lattice contribution of aT^3 from C_P, where $a \approx 1.056 \times 10^{-3}$ cal/mol-K^4.

the physical behaviour. The dashed line denotes the raw experimental magnetic specific heat C_P while the circles denote the experimental data, already corrected for a lattice contribution aT^3 with $a \approx 1.056 \times 10^{-3}$ cal/mol K^4 [43]. In the absence of a magnetic field a rounded peak, indicating short range ordering, is predicted around 0.23 K from the HTE result. Below $T \approx 0.23$ K, there is an exponential decay due to an ordered phase.

3.2. The compound NENC

It is known that antiferromagnetic spin-1 chains [34, 35, 36] with weak planar anisotropy can exhibit a non-magnetic Haldane phase. The large D gapped phase has been observed in the compounds NENC, NDPK and NBYC [46, 49]. In these compounds the in-plane anisotropy $x^2 - y^2$ breaks the z^2 symmetry and weakens the planar anisotropy effect. It was inferred from the experimental analysis in NENC [46] that the contribution E from the in-plane anisotropy is negligible in comparison with large D, where the Nickel(II) z^2 orbit along the c-axis forms a strong crystalline field. As a result this strong crystalline field dominates the low temperature physics. The antiferromagnetic intrachain exchange interaction further lowers the energy but its contribution to the ground state, as well as the low-lying excitations, is minimal. As a consequence, the model (2) with appropriate single-ion anisotropy is expected to describe this compound rather well. The specific
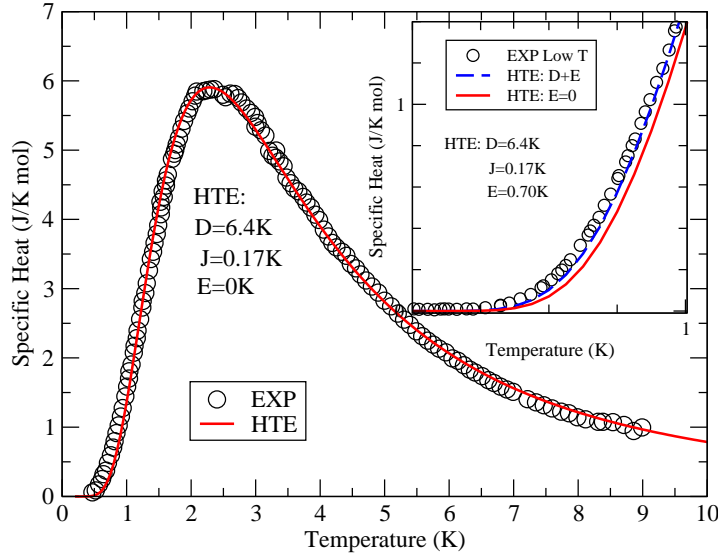
Figure 10. Comparison between theory and experiment [46] for the magnetic specific heat versus temperature of the compound $Ni(C_2H_8)_2Ni(CN)_4$ (NENC). The conversion constant is $C_{HTE} \approx 8C_{EXP}$ (J/mol-K). The solid line denotes the specific heat evaluated directly from the free energy with the parameters $J = 0.17$ K, $D = 6.4$ K, $E = 0$ with $g = 2.24$ and $\mu_B = 0.672$ K/T. The low temperature specific heat curves are shown in the inset. For low temperatures the inclusion of in-plane rhombic anisotropy $E = 0.7$ K (dashed line) gives a better fit than without rhombic anisotropy (solid line).

heat has been measured up to a temperature around 10 K [46]. A typical round peak for short range ordering at $T \approx 2.4$ K is observed (see Figure 10). An exponential decay is detected for temperatures below approx. 2.4 K. The calculated HTE specific heat evaluated from the model (2) with $J = 0.17$ K, $D = 6.4$ K (the solid line with $E = 0$ in Figure 10) is in excellent agreement with the experimental curve in the temperature region $T > 0.8$ K. Our analytic result for the specific heat gives a better fit with the experimental data than the perturbation theory prediction [46]. For low temperatures (below 0.8 K) paramagnetic impurities and a small rhombic distortion are the main reasons for the discrepancy. The inset of Figure 10 shows that the addition of a small rhombic anisotropy $E = 0.7$ K (dashed line) gives a better fit at low temperatures than that with $E = 0$ (solid line). However, it is negligible for high temperatures.

As far as we know the susceptibility measurement for this compound was made on powdered samples in a small magnetic field of $H = 0.1$ mT. The electron spin resonance for this compound was studied in Ref. [48]. In Figure 11, we compare the experimental results with our theoretical predictions. The susceptibility of NENC was measured only in the temperature range 50 mK - 18 K. From the data provided in Ref. [46] we could not accurately estimate constants for the Curie-Weiss term or the paramagnetic impurities.
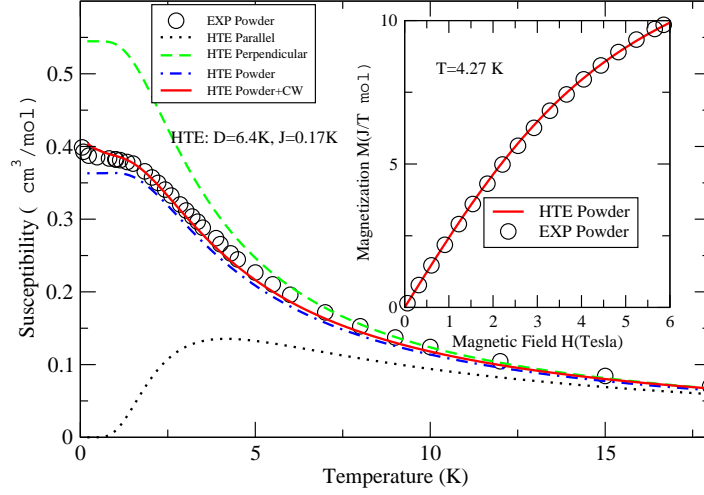
Figure 11. Comparison between theory and experiment [47] for the susceptibility versus temperature of the compound NENC. The theoretical curve (solid line) is obtained via the empirical relation $\chi_{\text{Powder}} = \frac{1}{3}\chi_\| + \frac{2}{3}\chi_\perp$ and by adding a Curie-Weiss contribution. The inset shows the comparison for magnetization versus magnetic field at $T = 4.27$ K. The theoretical curve follows from the empirical expression for the powder magnetization. A fit for the susceptibility and magnetization suggests the coupling constants $J = 0.17$ K, $D = 6.4$ K and $E = 0$, with $g_\perp = 2.18$ and $g_\| = 2.24$. The conversion constants are the same as in the previous figure Figure 8.

The theoretical HTE curves for the susceptibility with both parallel and perpendicular magnetic field are again evaluated from the free energy (44) with chemical potential terms (9) and (10). We obtained the powder susceptibility from the heuristic average

$$\chi_{\text{Powder}} = \tfrac{1}{3}\chi_\| + \tfrac{2}{3}\chi_\perp. \tag{54}$$

In this form it does not fit the experimental data very well at low temperatures, probably due to small contributions from a Curie-Weiss term and paramagnetic impurities. We have corrected the powder susceptibility χ_{Powder} with the Curie-Weiss contribution $c/(T - \theta)$ to obtain a better agreement with the experimental curves. Here $c \approx 0.045$ cm^3 K/mol and $\theta \approx -0.9$ K. For our spin chain model, the CW-corrected experimental data suggests the fitted coupling constants $J = 0.17$ K, $D = 6.4$ K and $E = 0$, with $g_\perp = 2.18$ and $g_\| = 2.24$. In this case the TBA analysis predicts an energy gap $\Delta \approx 5.72$ K for a parallel external magnetic field. The inset of Figure 11 shows the magnetization of a powder sample at $T = 4.27$ K. The singlet is supressed by the temperature. The best agreement between the experimental data and our powdered magnetization, $M_{\text{Powder}} = \frac{1}{3}M_\| + \frac{2}{3}M_\perp$, is found with the anisotropic Lande factors $g_\perp = 2.18$ and $g_\| = 2.24$. Here $M_\|$ and $M_\perp$ denote the magnetization for the external field parallel and perpendicular to the axis of quantization.

3.3. The compound NBYC

In this section we discuss the application of our theoretical results to measurements done on the spin-1 compound [49] $Ni(C_{10}H_8N_2)_2Ni(CN)_4 \cdot H_2O$ (NBYC). For this compound it is generally believed that the in-plane anisotropy E and the large anisotropy D play a significant role and so we expect the integrable model (2) with suitable on-site anisotropy interactions to be a good microscopic model for this material.

The thermodynamic properties have recently been experimentally investigated in Ref. [49]. Theoretical studies based on a strong-coupling expansion method [62] suggest that the anisotropy of this compound might lie close to the boundary between the observed Haldane and field-induced gapped phases [49]. However, due to the validity of the strong-coupling expansion method [49], there are apparent descrepancies in fitting the specific heat, susceptibility and magnetization if the rhombic anisotropy is large. Here we evaluate the relevant quantities for the powdered samples using the free energy expression (44) with parallel and perpendicular magnetic fields, in-plane anisotropy E and single-ion anisotropy D (see (9) and (10) and their eigenvalues (12a)-(12f)) via the empirical formula $\chi_{\text{Powder}} = \frac{1}{3}\chi_{\parallel} + \frac{2}{3}\chi_{\perp}$.

In Figure 12 we compare the results for the susceptibility of NBYC. A fit for the susceptibility suggests the coupling strengths $D = 2.62$ K, $E = 1.49$ K and $J = 0.35$ K, with $g_{\parallel} = g_{\perp} = 2.05$. The small discrepancy at low temperature is probably caused by a Curie-Weiss contribution. The inset of Figure 12 shows plots of the magnetization of the powdered samples at T=5, 10, 20 K. Again our theoretical curves are evaluated from the empirical relation $M_{\text{Powder}} = \frac{1}{3}M_{\parallel} + \frac{2}{3}M_{\perp}$. An overall agreement for the magnetization at different temperatures is consistent with the parameters used for the susceptibility. The singlet state is now supressed by both the in-plane rhombic anisotropy and the temperature.

We turn now to the specific heat which has been measured up to a temperature of 6 K [49]. The theoretical specific heat evaluated from the integrable model (2), with the same parameters given above, is in good agreement with the experimental data in the temperature region 0.5 K to 6 K, as can be seen in Figure 13. For lower temperatures the HTE does not give reliable results due to poor convergence.

3.4. The compound NDPK

Another compound considered in Ref. [46] to be a spin-1 magnetic chain with planar and in-plane anisotropy is NDPK. As far as we are aware, there has been no comprehensive theoretical and experimental study of this compound. The specific heat of NDPK was measured only in the temperature range from 100 mK to 2.5 K. A numerical ESCA study [46] of the specific heat indicated this compound lies in the large-D phase. Quantitative agreement with the experimental data suggested the values $D = 5$ K, $J = 0.96$ K and $E = 2.8$ K [46]. We examined the specific heat via the integrable model (2) with the parameters $D = 5.15$ K, $J = 0.55$ K and $E = 2.55$ K. The specific heat (solid line) evaluated from the HTE is in good agreement with experimental data in the temperature
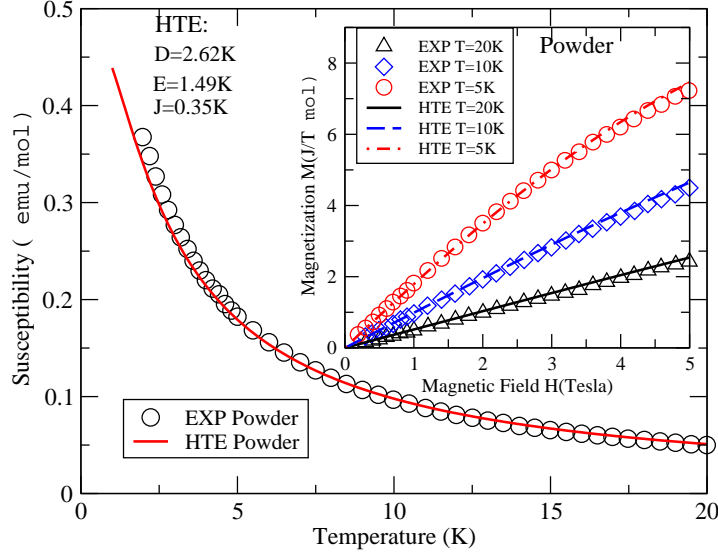
Figure 12. Comparison between theory and experiment [49] for the susceptibility versus temperature of the spin-1 chain compound NBYC. The conversion constants are the same as for the above materials. The solid line is the susceptibility evaluated directly from the free energy of the spin-1 chain for the powdered samples with coupling constants $J = 0.35$ K, $D = 2.62$ K and $E = 1.49$ K, with $g_\parallel = g_\perp = 2.05$. The small discrepancy at low temperature might be attributed to a Cuire-Wess contribution. The inset shows the magnetization for the powder samples at T=5, 10, 20 K.

region 0.9 K to 2.5 K (see Figure 14). For temperatures below 1 K, the HTE is not valid due to the small ratio of J/T. We believe that the integrable model will also describe other magnetic properties of NDPK.

4. The integrable spin-$\frac{3}{2}$ chain

4.1. The exactly solved $su(4)$ model

It is generally believed that the ground state of the antiferromagnetic spin-S Heisenberg chain remains in a gapless phase when $2S$ is an odd integer [29, 31]. Nevertheless, an appropriate projection operator can open a "Haldane gapped phase" [30]. Numerical study [61] of the spin-$\frac{3}{2}$ antiferromagnetic chain has verified the existence of a one third saturation magnetization plateau. In this section we consider an integrable spin-$\frac{3}{2}$ chain with two different kinds of single-ion anisotropies, capable of triggering gapped and gapless phases. We investigate the thermodynamics of the model in terms of the HTE and TBA. The two Hamiltonians in the fundamental basis are given by

$$\mathcal{H} = J \sum_{j=1}^{L} P_{j,j+1}^{(3)} + D \sum_{j=1}^{L} P_j^\pm - \mu_B g H \sum_{j=1}^{L} S_j^z, \tag{55}$$
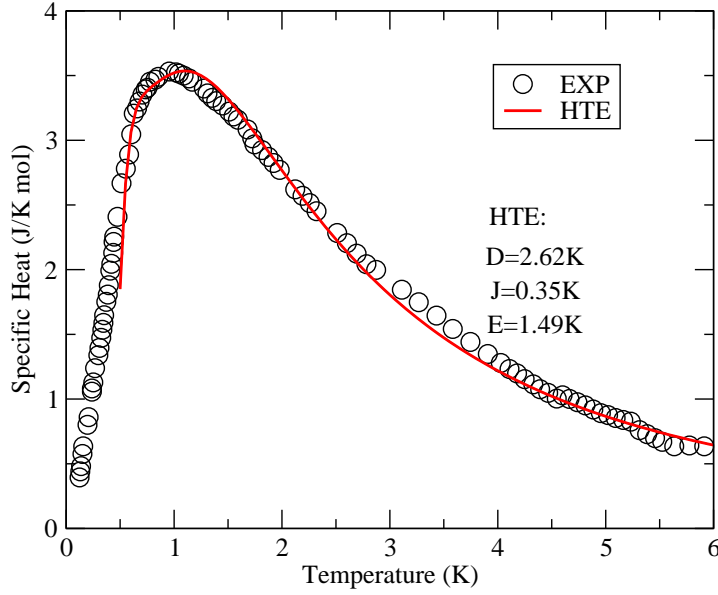
Figure 13. Comparison between theory and experiment [49] for the magnetic specific heat versus temperature of the compound NBYC. The conversion constant is $C_{\mathrm{HTE}} \approx 10 C_{\mathrm{EXP}}$ (J/mol-K). The solid line denotes the specific heat at $H = 0.1$ mT evaluated directly from the free energy with parameters $D = 2.62$ K, $E = 1.49$ K and $J = 0.35$ K, with $g = 2.05$ and $\mu_B = 0.672$ K/T.

where

$$P_{j,j+1}^{(3)} = \sum_{\alpha=0}^{2} (-1)^{2-\alpha} \prod_{\beta \neq \alpha}^{2} \frac{\vec{S}_j \cdot \vec{S}_{j+1} - x_\beta}{x_\alpha - x_\beta}, \tag{56}$$

with $x_\alpha = \frac{1}{2}\alpha(\alpha+1) - S(S+1)$ [53]. We define model 1 with projection operator P^+ and model 2 with P^-, where

$$
\begin{aligned}
P_j^+ &= (S_j^z + \tfrac{3}{2})(S_j^z - \tfrac{3}{2})(S_j^z + \tfrac{1}{2}), \\
P_j^- &= (S_j^z)^2.
\end{aligned} \tag{57}
$$

In the above, $\vec{S}_j$ is the spin-$\frac{3}{2}$ operator acting on site j, J is the exchange coupling and D is the single-ion anisotropy. The operator P_j^+ projects spin states onto the state with $M^z = \frac{1}{2}$, which leads to a magnetic ground state. In general, one can incorporate different projection operators in the spin-S chain associated with the integrable $su(n)$ model with $n = 2S + 1$ [56] such that multi-plateaux phases can occur.
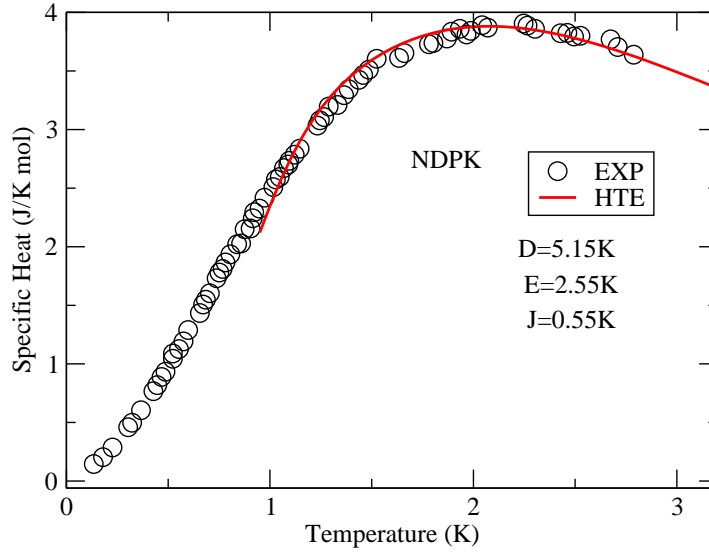
Figure 14. Comparison between theory and experiment [46] for the magnetic specific heat versus temperature of the compound NDPK. The conversion constant is $C_{\text{HTE}} \approx 10 C_{\text{EXP}}$ (J/mol-K). The solid line denotes the specific heat at $H = 0$ T evaluated directly from the free energy with the parameters $D = 5.15$ K, $E = 2.55$ K and $J = 0.55$ K.

4.2. HTE approach

To investigate the thermodynamic properties we again apply the HTE scheme. The eigenvalue of the QTM (up to a constant) is [54, 15]

$$
\begin{aligned}
T_1^{(1)}\left(v, \left\{v_i^{(a)}\right\}\right) = {} & e^{-\beta\mu_1} \phi_-(v - i)\phi_+(v) \frac{Q_1(v + \frac{1}{2}i)}{Q_1(v - \frac{1}{2}i)} \\
& + e^{-\beta\mu_2} \phi_-(v)\phi_+(v) \frac{Q_1(v - \frac{3}{2}i)Q_2(v)}{Q_1(v - \frac{1}{2}i)Q_2(v - i)} \\
& + e^{-\beta\mu_3} \phi_-(v)\phi_+(v) \frac{Q_2(v - 2i)Q_3(v - \frac{1}{2}i)}{Q_2(v - i)Q_3(v - \frac{3}{2}i)} \\
& + e^{-\beta\mu_4} \phi_-(v)\phi_+(v + i) \frac{Q_3(v - \frac{5}{2}i)}{Q_3(v - \frac{3}{2}i)}.
\end{aligned}
\tag{58}
$$

In the above equations, μ_i, $i = 1, 2, 3, 4$, are the eigenvalues of the on-site chemical potentials with regard to the fundamental basis $|S^z\rangle$

$$
|1\rangle = |\tfrac{3}{2}\rangle, \ |2\rangle = |\tfrac{1}{2}\rangle, \ |3\rangle = |-\tfrac{1}{2}\rangle, \ |4\rangle = |-\tfrac{3}{2}\rangle.
\tag{59}
$$

For model 1 with projection operator P^+ the chemical potentials are

$$
\begin{aligned}
\mu_1 &= -\tfrac{3}{2}\mu_B gH, & \mu_2 &= -\tfrac{1}{2}\mu_B gH - 2D, \\
\mu_3 &= \tfrac{1}{2}\mu_B gH, & \mu_4 &= \tfrac{3}{2}\mu_B gH.
\end{aligned}
\tag{60}
$$

For model 2 with projection operator P^- the chemical potentials are

$$\mu_1 = -\tfrac{3}{2}\mu_B g H, \qquad \mu_2 = -\tfrac{1}{2}\mu_B g H - 2D,$$
$$\mu_3 = \tfrac{1}{2}\mu_B g H - 2D, \quad \mu_4 = \tfrac{3}{2}\mu_B g H. \tag{61}$$

The HTE expansion of the free energy, up to third order, is given by

$$-\frac{1}{T}f(T,H) = \ln Q_1^{(1)} + C_{1,0}^1 \left(\frac{J}{T}\right) + C_{2,0}^1 \left(\frac{J}{T}\right)^2 + C_{3,0}^1 \left(\frac{J}{T}\right)^3 + \cdots. \tag{62}$$

where now [15]

$$c_{1,0}^{(1)} = 2\frac{Q_1^{(2)}}{Q_1^{(1)^2}},$$

$$c_{2,0}^{(1)} = 3\frac{Q_1^{(2)}}{Q_1^{(1)^2}} - 6\frac{Q_1^{(2)^2}}{Q_1^{(1)^4}} + 3\frac{Q_1^{(3)}}{Q_1^{(1)^3}},$$

$$c_{3,0}^{(1)} = \frac{10}{3}\frac{Q_1^{(2)}}{Q_1^{(1)^2}} - 18\frac{Q_1^{(2)^2}}{Q_1^{(1)^4}} + \frac{80}{3}\frac{Q_1^{(2)^3}}{Q_1^{(1)^6}} + 8\frac{Q_1^{(3)}}{Q_1^{(1)^3}} - 24\frac{Q_1^{(2)}Q_1^{(3)}}{Q_1^{(1)^5}} + 4\frac{Q_1^{(4)}}{Q_1^{(1)^4}}.$$

Here the Q-system for $su(4)$ is

$$Q_1^{(1)} = e^{-\beta\mu_1} + e^{-\beta\mu_2} + e^{-\beta\mu_3} + e^{-\beta\mu_4},$$
$$Q_1^{(2)} = e^{-\beta\mu_1-\beta\mu_2} + e^{-\beta\mu_1-\beta\mu_3} + e^{-\beta\mu_1-\beta\mu_4} + e^{-\beta\mu_2-\beta\mu_3} + e^{-\beta\mu_2-\beta\mu_4} + e^{-\beta\mu_3-\beta\mu_4},$$
$$Q_1^{(3)} = e^{-\beta\mu_1-\beta\mu_2-\beta\mu_3} + e^{-\beta\mu_1-\beta\mu_2-\beta\mu_4} + e^{-\beta\mu_1-\beta\mu_3-\beta\mu_4} + e^{-\beta\mu_2-\beta\mu_3-\beta\mu_4},$$
$$Q_1^{(4)} = e^{-\beta\mu_1-\beta\mu_2-\beta\mu_3-\beta\mu_4}.$$

4.3. TBA analysis: ground state properties and magnetization plateau

First consider Hamiltonian (55) with projection operator P^+. The anisotropy terms $P^\pm$ and the external field can be diagonalized simultaneously in the fundamental basis (59). If $D > 0$, the projection operator P_j^+ energetically favours the component $|2\rangle$. Proceding in an analogous fashion to the spin-1 TBA analysis, we find that the magnetic ground state is separated from the lowest magnon excitation by the gap $\Delta = 2D - 4J$ in the zero temperature limit. A magnetization plateau with $M = \tfrac{1}{2}$ starts from zero field. The gap is diminished by the magnetic field. If the magnetic field is larger than the critical field $H_{c1} = (2D - 4J)/\mu_B g$, a phase transition from a ferrimagnetic phase to an antiferromagnetic phase occurs. As the magnetic field increases, the magnetization almost linearly increases up to the saturation magnetization. The saturation critical field is $H_{c2} = (2D + 4J)/\mu_B g$. The magnetization and the susceptibility evaluated from the free energy (62) with the chemical potentials given by (60) are shown in parts (A) and (A') of Figure 15. The magnetization curve indicates that the ground state remains gapped until the magnetic field exceeds the critical field H_{c1}. A round peak is found in the susceptibility. This conclusion coincides with the suggestion by Masaki et al. [30] that the gapped phase might exist in the $2S$ odd integer antiferromagnetic spin chains.

Apart from this degenerate ground state, there also exists another gapped $M = \tfrac{1}{2}$ magnetization plateau in the spin-$\tfrac{3}{2}$ chain. If we consider the Hamiltonian (55) with

a large anisotropy term P^-, the ground state lies in a gapless phase. The gapless ground state could be shifted into the gapped phase with a magnetization plateau $M = \frac{1}{2}$. The field-induced magnetic effects occur as follows: (i) the system undergoes a phase transition from an antiferromagnetic phase into a ferrimagnetic phase at the critical point $H_{c1} = 4J/\mu_B g$; (ii) the $M = \frac{1}{2}$ magnetization plateau vanishes at $H_{c2} = (2D - 4J)/\mu_B g$; (iii) the ground state is fully-polarized beyond the critical field $H_{c3} = (2D + 4J)/\mu_B g$. The magnetization curve given in part (B) of Figure 15 indicates the existence of a mid-plateau, which is reminiscent of the mixed spin-$(1, \frac{1}{2})$ ladder [23]. Remarkably, with regard to this mid-plateau, a cusp-like phase transition emerges in the susceptibility curve in (B') of Figure 15. This field-induced cusp is similar to the spin-Peierls transition in spin-$\frac{1}{2}$ chain materials [28]. We anticipate that this novel phase transition may exist in real spin-$\frac{3}{2}$ chain compounds.

5. Conclusion

We have studied the thermal and magnetic properties of spin-1 and spin-$\frac{3}{2}$ chains via the $su(3)$ and $su(4)$ integrable models. This has enabled some novel phase transitions and critical behaviour to be predicted via the TBA analysis and HTE method. In particular, the zero temperature TBA predictions and the temperature-dependent analytic result derived from the HTE provide the full ground state properties and thermodynamics of the underlying models. The integrable spin-1 model with appropriate chemical potentials gives a good description of some real spin-1 chain compounds with large single-ion anisotropy. The planar anisotropy on-site interaction leads to a gapped phase which is significantly different from the Haldane phase in which the spin-spin exchange interaction results in a valence bond solid ground state. We have compared the theoretical curves with measurements on spin-1 chain compounds such as the Nickel salt $NiSnCl_6 \cdot 6H_2O$ (section 3.1), NENC (section 3.2), NBYC (section 3.3), NDPK (section 3.4). In general, the agreement with the experimental data for the compounds under comparison is excellent. Moreover, a specific anisotropy in the spin-1 chain can trigger a mid-plateau which causes a spin-Peierls-like quantum phase transition.

We have considered two types of on-site anisotropies for the integrable spin-$\frac{3}{2}$ chain. In contrast to the non-magnetic gapped phase in the spin-1 chain, the magnetic gapped ground state can be separated from the lowest magnon excitation in the integrable spin-$\frac{3}{2}$ chain. Counting the magneitzation plateau in units of the saturation value $M_s = \frac{3}{2}$, a one third magnetization plateau with $M = \frac{1}{2}$ can start at zero magnetic field. Moreover, an appropriate single-ion anisotropy can open a one third mid-magnetization plateau as also exhibited in the mixed spin-$(1, \frac{1}{2})$ ladder model [23]. We anticipate that the one third magnetization plateau may be observed in some real spin-$\frac{3}{2}$ compounds.
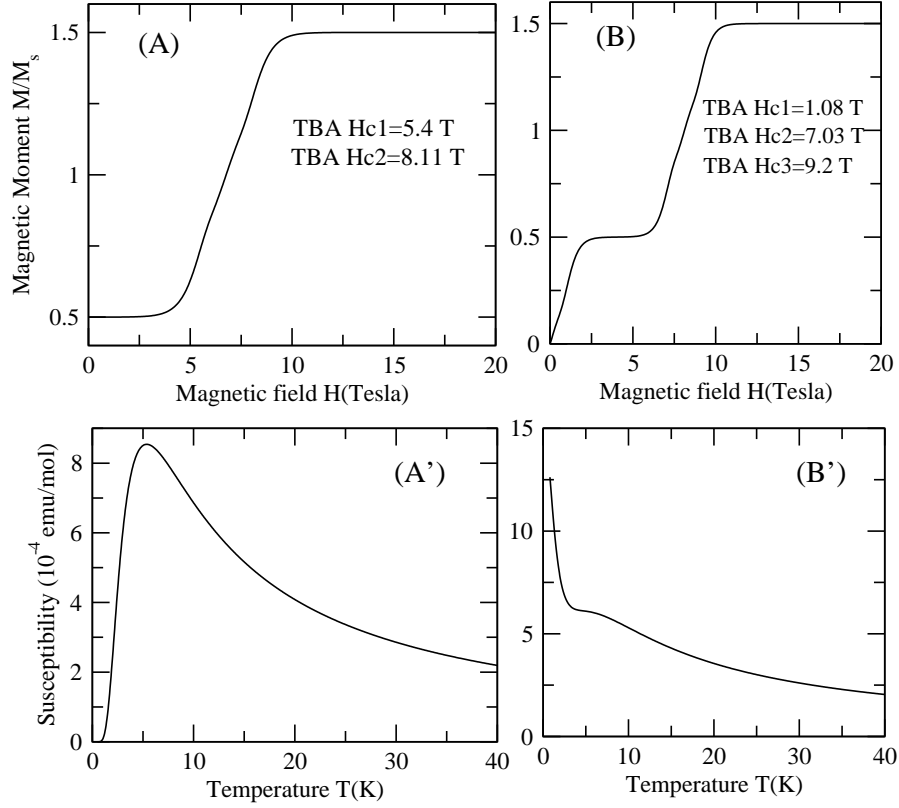
Acknowledgments

Figure 15. Theoretical curves for the spin-$\frac{3}{2}$ chain model (55) with single-ion anisotropy. Parts (A) and (B) show the magnetization versus magnetic field at $T = 0.8$K. In part (A) $D = 5$ K and $J = 0.5$ K which suggests a magnetic gapped ground state for the Hamiltonian (55) with projection operator P^+. In part (B) $D = 6$ K and $J = 0.4$ K which suggests a gapless ground state for the Hamiltonian (55) with the single-ion anisotropy P^-. We have set $\mu_B = 0.672$ K/T and $g = 2.20$. The critical fields estimated from the magnetization curves coincide with the TBA results. Parts (A') and (B') show the susceptibility versus temperature at $H = 0$ T. The numerical values in (A') and (B') are the same as in parts (A) and (B), respectively. The susceptibility curves in (A') indicate the existence of an energy gap, whereas no significant gap can be observed in figure (B'), however, the mid-plateau suggests a spin-Peierls-like quantum phase transition.

References

[1] McGuire J B 1964 *J. Math. Phys.* **5** 622
[2] Yang C N 1967 *Phys. Rev. Lett.* **19** 1312
[3] Baxter R J 1972 *Ann. Phys., NY* **70** 193
[4] Uimin G V 1970 *JETP Lett.* **12** 225
[5] Sutherland B 1975 *Phys. Rev.* B **12** 3795
[6] Bazhanov V V 1985 *Phys. Lett.* B **159** 321
[7] Jimbo M 1986 *Comm. Math. Phys.* **102** 537
[8] Perk J H H and Schultz C L 1981 *Phys. Lett.* A **84** 407
[9] Baxter R J 1982 *Exactly Solved Models in Statistical Mechanics* (London: Academic Press)
[10] Jimbo M and Miwa T 1995 *Algebraic Analysis of Solvable Models* CBMS Number 85
[11] Takahashi M 1999 *Thermodynamics of One-Dimensional Solvable Models* (Cambridge: Cambridge University Press)
[12] Yang C N and Yang C P 1969 *J. Math. Phys.* **10** 1115
[13] Takahashi M 1971 *Prog. Theor. Phys.* **46** 401
[14] Shiroishi M and Takahashi M 2002 *Phys. Rev. Lett.* **89** 117201
[15] Tsuboi Z 2003 *J. Phys. A: Math. Gen.* **36** 1493
[16] Suzuki M 1985 *Phys. Rev.* B **31** 2957
  Klümper A 1992 *Ann. Physik* **1** 540
  Jüttner G, Klümper A and Suzuki J 1997 *Nucl. Phys.* B **487** 650
[17] Klümper A 1993 *Z. Physik* B **91** 507
[18] Kuniba A, Nakanishi T and Suzuki J 1994 *Int. J. Mod. Phys.* A **9** 5215
  ——1994 *Int. J. Mod. Phys.* A **9** 5267
[19] Tsuboi Z 2004 *J. Phys. A: Math. Gen.* **37** 1747
[20] Batchelor M T, Guan X-W, Oelkers N, Sakai K, Tsuboi Z and Foerster A 2003 *Phys. Rev. Lett.* **91** 217202
[21] Ying Z-J, Roditi I, Foerster A and Chen B, cond-mat/0403520
  Ying Z-J, Roditi I and Zhou H-Q, cond-mat/0405274
[22] Batchelor M T, Guan X-W, Foerster A and Zhou H-Q 2003 *New J. Phys.* **5** 107
  ——2003 *Nucl. Phys.* B **669** 385
[23] Batchelor M T, Guan X-W, Oelkers N and Ying Z-J 2004 *J. Stat. Phys.* **116** 571
[24] Ying Z-J, Foerster A, Guan X-W, Chen B and Roditi I 2004 *Eur. Phys. J.* B **38** 535
  Ying Z-J, Guan X-W, Foerster A, Roditi I and Chen B, cond-mat/0309718
[25] Batchelor M T, Guan X-W and Oelkers N 2004 *Phys. Rev. B* in press
[26] Dagotto E and Rice T M 1996 *Science* **271** 618
  Dagotto E 1999 *Rep. Prog. Phys.* **62** 1525
[27] Kodama K *et al* 2002 *Science* **298** 395
[28] Hase M, Terasaki I and Uchinokura K 1993 *Phys. Rev. Lett.* **70** 3651
  Pashchenko V A, Sulpice A, Mila F, Millet P, Stepanov A and Wyder P 2001 *Eur. Phys. J.* B **21** 473
[29] Haldane F D M 1983 *Phys. Lett.* A **93** 464
  ——1983 *Phys. Rev. Lett.* **50** 1153
[30] Oshikawa M, Yamanaka M and Affleck I 1997 *Phys. Rev. Lett.* **78** 1984
[31] Affleck I 1989 *Phys. Rev. Lett.* **62** 474
  Affleck I 1990 *Phys. Rev.* B **41** 6697
  Affleck I, Kennedy T, Lieb E H and Tasaki H 1987 *Phys. Rev. Lett.* **59** 799
[32] Tsvelik A M 1990 *Phys. Rev.* B **42** 10499
[33] Affleck I 1989 *J. Phys. Condens. Matter* **1** 3047
[34] Ajiro Y, Goto T, Kikuchi H, Sakakibara T, Inami T 1990 *J. Magn. and Mag. Mat.* **90** & **91** 231
  Hirota K, Shapiro S M, Katsumata K and Hagiwara M, 1995 *Physica* B **213** & **214** 173

Renard J P, Verdaguer M, Regnault L P, Erkelens W A C, Rossat-Mignod J, Ribas J, Stirling W G and Vettier C 1988 *J. Appl. Phys.* **63** 3538

[35] Honda Z, Asakawa H and Katsumata K 1998 *Phys. Rev. Lett.* **81** 2566

Honda Z, Katsumata K, Nishiyama Y and Harada I 2001 *Phys. Rev.* Phys. Rev. **63** 064420

Renard J P, Gadet V, Regnault L P, Verdaguer M 1990 *J. Magn. Magn. Mater.* **90** & **91** 213

[36] Katsumata K, Hori H, Takeuchi T, Date M, Yamagishi A and Renard J P 1989 *Phys. Rev. Lett.* **63** 86

[37] Hagiwara M 2002 *Mol. Phys.* **100** 1489

[38] Gavilano JL, Mushkolaj S, Ott HR, Millet P and Mila F 2000 *Phys. Rev. Lett.* **85** 409

Millet P *et al* 1999 *Phys. Rev. Lett.* **83** 4176

[39] Lumsden M D *et al* 2000 *Phys. Rev.* B **62** R9244

[40] Vonlanthen P *et al* 2002 *Phys. Rev.* B **65** 214413

[41] Lou JH, Xiang T and Su ZB 2000 *Phys. Rev. Lett.* **85** 2380

[42] Schollwöck U, Jolicoeur Th and Garel T 1996 *Phys. Rev.* B **53** 3304

[43] Myers B E, Polgar L G and Friedberg S A 1972 *Phys. Rev.* B **6** 3488

[44] Carlin R L, O'Connor C J and Bhatia S N 1976 *J. Am. Chem. Soc.* **98** 3523

[45] Herweijer A and Friedberg S A 1971 *Phys. Rev.* B **4** 4009

[46] Feher A, Orendáč M, Orendáčová A and Čižmár E 2002 *Low Temp. Phys.* **28** 551

Orendáč M, Orendáčová A, Černák J, Feher A, Signore P J C, Meisel M W, Merah S and Verdaguer M 1995 *Phys. Rev.* B **52** 3435

[47] Orendáč M *et al* 1995 *J. Magn. Magn. Mater.* **140-144** 1643

[48] Kolezhuk A K and Mikeska H J 2001 *Phys. Rev.* B **65** 014413

Orendáč M *et al* 1999 *Phys. Rev.* B **60** 4170

[49] Orendáč M *et al* 2000 *Phys. Rev.* B **61** 3223

[50] Carlin R L 1986 *Magnetochemistry* (Springer-Verlag, New York)

[51] Milla F 2000 *Eur. J. Phys.* **21** 499

[52] Huang H and Affleck I, cond-mat/0401158

[53] Kennedy T 1992 *J. Phys. A: Math. Gen.* **25** 2809

Batchelor M T and Yung C M 1994 *J. Phys. A: Math. Gen.* **27** 5033

—— 1995 Integrable $su(2)$ invariant spin chains and the Haldane conjecture, in *Confronting the Infinite* eds A L Carey *et al* (Singapore: World Scientific) pp 167-174

[54] Fujii A and Klümper A 1999 *Nucl. Phys.* B **546** 751

[55] Martins M J and Ramos P B 1997 *Nucl. Phys.* B **500** 579

[56] de Gier J, Batchelor M T and Maslen M 2000 *Phys. Rev.* B **61** 15196

de Gier J and Batchelor M T 2000 *Phys. Rev.* B **62** R3584

Batchelor M T, de Gier J and Maslen M 2001 *J. Stat. Phys.* **102** 559

Maslen M, Batchelor M T and de Gier J 2003 *Phys. Rev.* B **68** 024418

[57] Takahashi M 1972 *Prog. Theor. Phys.* **47** 69

[58] Schlottmann P 1997 *Int. J. Mod. Phys.* B **11** 355

Schlottmann P 1986 *Phys. Rev.* B **33** 4880

[59] Tsvelik A M and Wiegmann P B 1983 *Adv. in Phys.* **32** 453

[60] Johnston D C *et al* cond-mat/0001147

[61] Kitazawa A and Okamoto K 2000 *Phys. Rev.* B **62** 940

Refael G, Kehrein S and Fisher D S 2002 *Phys. Rev.* B **66** 060402(R)

Sakai T and Takahashi M 1998 *Phys. Rev.* B **57** 3201(R)

[62] Papanicolaou N and Spathis P N 1995 *Phys. Rev.* B **52** 16001